Synthesis, structure and spectroscopy of Fe2+:MgAl2O4 transparent ceramics and glass-ceramics

Liza Basyrova, Vasilisa Bukina, Stanislav Balabanov, Alexander Belyaev, Viktor Drobotenko, Olga Dymshits, Irina Alekseeva, Marina Tsenter, Svetlana Zapalova, Alexander Khubetsov, et al.

To cite this version:

Liza Basyrova, Vasilisa Bukina, Stanislav Balabanov, Alexander Belyaev, Viktor Drobotenko, et al.. Synthesis, structure and spectroscopy of Fe2+:MgAl2O4 transparent ceramics and glass-ceramics. Journal of Luminescence, 2021, 236, pp.118090. 10.1016/j.jlumin.2021.118090 . hal-03215579

HAL Id: hal-03215579
https://hal.science/hal-03215579

Submitted on 24 Apr 2023

Synthesis, structure and spectroscopy of Fe^{2+}:$MgAl_2O_4$ transparent ceramics and glass-ceramics

Liza Basyrova[a], Vasilisa Bukina[b], Stanislav Balabanov[c], Alexander Belyaev[c], Viktor Drobotenko[c], Olga Dymshits[d], Irina Alekseeva[d], Marina Tsenter[d], Svetlana Zapalova[d], Alexander Khubetsov[d], Alexander Zhilin[d], Anna Volokitina[a], Vladimir Vitkin[a], Xavier Mateos[e], Josep Maria Serres[e], Patrice Camy[f], and Pavel Loiko[f,*]

[a]*ITMO University, Kronverkskiy pr., 49, 197101 Saint-Petersburg, Russia*
[b]*Saint Petersburg Mining University, 2 21st Line Vasil'yevski Ostrov, Saint Petersburg, Russia*
[c]*G.G. Devyatykh Institute of Chemistry of High-Purity Substances, RAS, 49 Tropinin St., 603951 Nizhny Novgorod, Russia*
[d]*Vavilov State Optical Institute, 36 Babushkina St., 192171 St. Petersburg, Russia*
[e]*Física i Cristal·lografia de Materials i Nanomaterials (FiCMA-FiCNA)-EMaS, Dept. Química Física i Inòrganica, Universitat Rovira i Virgili (URV), Campus Sescelades, E-43007 Tarragona, Spain*
[f]*Centre de recherche sur les Ions, les Matériaux et la Photonique (CIMAP), UMR 6252 CEA-CNRS-ENSICAEN, Université de Caen Normandie, 6 Boulevard du Maréchal Juin, 14050 Caen Cedex 4, France*

**Corresponding author, e-mail: kinetic@tut.by, pavel.loiko@ensicaen.fr*

ABSTRACT. We report on a comparative study of a transparent Fe:$MgAl_2O_4$ (spinel) ceramics and a transparent nanophase Fe:$MgAl_2O_4$-based glass-ceramics. The 0.1 mol% Fe:$MgAl_2O_4$ ceramics was synthesized by hot pressing (at 1500 °C / 50 MPa) of powders obtained by the sol-gel method using LiF as a sintering aid. The Fe:$MgAl_2O_4$ ceramic is a single-phase material (cubic structure, sp. gr. $Fd\bar{3}m$, a = 8.083 Å) with a mean grain size of ~50 µm. The ceramic exhibits a broadband transparency of 0.2–6.0 µm and a high in-line transmission at ~1 µm of 74.4%. The iron ions are presented in the ceramics in the single state of Fe^{2+} species in tetrahedral (T_d) sites. A broad absorption band spanning from ~1.2 to 3.7 µm assigned to the $^5E \rightarrow {}^5T_2$ (^5D) transition of Fe^{2+} ions in T_d sites is observed, corresponding to a ground-state absorption cross section of 0.28×10^{-18} cm^2 at 1.90 µm. The glass-ceramics were prepared by secondary two-stage heat-treatments of the magnesium aluminosilicate glass nucleated by titanium oxide and doped with 0.1 mol% FeO. Transparent Fe:$MgAl_2O_4$-based glass-ceramics obtained at the temperature of the second stage of 800 – 1000 °C were multi-phase materials containing two crystalline nanophases, i.e., spinel (mean size: 3.7 – 7.4 nm) and magnesium aluminotitanate solid solution (mean size: 6.4 - 20.6 nm), as well as residual silica-rich glass. Glass-ceramics obtained at the temperature of the second stage of 1050 °C were transparent and based on Fe-doped sapphirine. For glass-ceramics, absorption has a much more complex character as it is caused by interplay of iron and titanium ions in different valence states, coordination sites and locations. The iron ions enter the spinel nanocrystals but unlike the ceramic, in the form of both $^{VI}Fe^{2+}$ and $^{IV}Fe^{2+}$ species. The developed ceramics and glass-ceramics are promising for saturable absorbers of mid-infrared (2-3 µm) lasers.

Keywords: transparent ceramics; glass-ceramics; spinel; iron ions; microstructure; spectroscopy.

1. Introduction

Divalent iron ions (Fe^{2+}) embedded in II-IV group materials such as ZnS and ZnSe are known for their intense and broadband absorption and emission in the mid-infrared originating from the $^5E \leftrightarrow {}^5T_2$ (^5D) transitions of Fe^{2+} ions in tetrahedral (T_d) crystal field [1]. For example, for Fe^{2+}:ZnSe, the maximum absorption is at 3.1 μm and the emission band is centered at 4.35 μm [2-4]. It makes Fe^{2+}-doped chalcogenides suitable for laser gain media [2,5,6] operating in this spectral range with multiple applications in gas sensing, molecular spectroscopy, range finding and medicine. Due to high ground-state absorption (GSA) cross sections for Fe^{2+} ions in T_d sites ($\sigma_{GSA} = 0.97\times10^{-18}$ cm^2 for Fe^{2+}:ZnSe) and the lack of excited-state absorption [1], Fe^{2+}-doped materials are also interesting for saturable absorbers (SAs) of mid-infrared lasers [4,7,8].

Because of relatively low hardness and laser-induced damage threshold (LIDT), high temperature coefficient of the refractive index of chalcogenides, and the lack of efficient pump lasers at a wavelength of 3.1 μm, it seems reasonable to find other hosts for Fe^{2+} ions doping. One of the possible host candidates is cubic magnesium aluminium spinel, $MgAl_2O_4$ [9]. This broad energy gap material features good thermal and mechanical properties (e.g., high Mohs hardness of 8, high thermal conductivity of 24.7 $Wm^{-1}K^{-1}$ for an undoped crystal [10] and relatively low thermal expansion coefficient of about 9×10^{-6} K^{-1} between 20 and 1200 °C [11]) together with a broad (for oxide crystals) transparency range of 0.2–5.5 μm. $MgAl_2O_4$ also exhibits high LIDT well exceeding that of chalcogenides. Spinel demonstrates widely variable occupation of two (tetrahedral, T_d, and octahedral, O_h) sites by various transition metal ions and distribution of the cations between these sites. $MgAl_2O_4$ is known for doping with such transition metal ions as Co^{2+}, Ni^{2+} and Cr^{3+} [12-14]. When doped with Co^{2+} ions entering predominantly in the T_d sites, it is recognized as a SA for eye-safe lasers operating at ~1.5 μm [15,16].

Iron-containing spinels are common in both the crust and the Earth's mantle, in meteorites, and in lunar rocks. There is a continuous solid solution between $MgAl_2O_4$, spinel, end-member and $FeAl_2O_4$, hercynite, end-member, which also has a normal spinel structure. It is not surprising that there exist structural and optical studies of iron-doped $MgAl_2O_4$ minerals. Andreozzi *et al.* studied the distribution of Fe^{2+} ions over the T_d and O_h sites in $MgAl_2O_4$ – $FeAl_2O_4$ solid solutions and revealed the tetrahedral preference of Fe^{2+} with respect to Mg^{2+} [17]. Gaffney described the spectra of Fe^{2+} ions in tetrahedral sites in spinel [18], based on an earlier work of Slack [19,20]. Taran *et al.* described optical absorption of natural (Fe^{3+},Fe^{2+})-bearing spinels [21]; a study of iron-bearing aluminate spinel under lunar-like redox conditions was performed by Jackson *et al.* [22]. Halenius *et al.* proposed a model of Fe^{2+}-Fe^{3+} ion pairs in spinels [23].

The melting point of $MgAl_2O_4$ is rather high (2135 °C). The single crystals are typically grown by the Czochralski method [24] using iridium crucibles which is challenging because the melting point of iridium is only slightly higher than that of spinel [25]. We found only one paper on Fe^{2+}-doped spinel single crystal [26] and one paper on growth of $FeAl_2O_4$, hercynite, single crystal [19]. According to Sackuvich *et al.* [26], Fe^{2+} ions in $MgAl_2O_4$ crystals feature broad absorption band with a maximum near 2 μm and a luminescence signal between 3 and 6 μm.

Thus, it is reasonable to propose other transparent $MgAl_2O_4$-based materials for doping with transition metal ions, namely, transparent polycrystalline ceramics [16] and transparent nanophase glass-ceramics (GCs) [27-29].

Nowadays, transparent ceramic technology is becoming competitive to traditional single crystal growth methods. It has several advantages [30], such as (i) lower synthesis temperature, (ii) size scalable production, (iii) easier doping with active ions, (iv) the development of compositions which are unstable / hardly reproducible in the single-crystalline form. At the same time, optical ceramics provide spectroscopic and thermal properties similar to those of single crystals. Optical quality of ceramics can be greatly improved by proper adjusting the synthesis procedure. Recently, multiple studies were dedicated to the development of transparent spinel ceramics, such as $MgAl_2O_4$ and $ZnAl_2O_4$ (gahnite) both undoped and Co^{2+}-doped [16,31-35]. For the consolidation of optical-quality spinel ceramics, either hot pressing with a fluoride-based sintering additive [36] or free sintering with a subsequent hot isostatic pressing (HIP) treatment is used [37]. Less frequent methods are spark plasma sintering (SPS) [38] and microwave sintering [39]. These methods allow to achieve high compaction rates and to preserve the sub-μm structure of ceramics which is responsible for their high micro-hardness. However, optical transmittance of such ceramics is usually lower due to incomplete pore removal during rapid compaction. Many methods in the preparation of spinel powders, such as sol-gel, solid-phase synthesis, pyrolysis of metal salts, *etc.*, have been developed [40]. The advantages of the sol-gel method of obtaining $MgAl_2O_4$ powders with the use of volatile metal alkoxides are high chemical purity of powders and a stable ratio of magnesium-to-aluminum ions of 1:2 [41]. High chemical purity of ceramics is an important requirement for their use in laser, terahertz and microwave technologies, especially for high-power applications [42,43].

Transparent nanophase GCs [44] are obtained by secondary heat-treatments of initial glasses of specially developed compositions. The initial glasses are produced by the melt-quenching technique, and they can be doped by active ions. As a result, the material contains nanosized crystals of one or several crystalline phases uniformly distributed in the residual glass. Fabrication of GCs is in many cases easier than that of transparent ceramics. GCs also benefit from higher LIDT [33]. However, it is important to control the distribution of active ions between the nanocrystalline phase (or phases) and the residual glass. Moreover, thermal conductivity of GCs is typically lower than that of optical ceramics. So far, multiple studies were dedicated to fabrication and characterization of spinel-based transparent GCs doped with Cr^{3+} [27,45], Co^{2+} [28,29] and Ni^{2+} ions [46-48].

In this work, we aim to fabricate and study the microstructure, vibronic and optical properties of novel transparent ceramics and GCs based on Fe^{2+}:$MgAl_2O_4$ spinel crystals. Previously, the authors from the Institute of Electrophysics UD RAS reported the development of transparent Fe^{2+}:$MgAl_2O_4$ ceramics [49-51]. The obtained ceramics [49-51] contained secondary oxide phase of $(MgO)_{0.91}(FeO)_{0.09}$ causing a substantial decrease in transmittance in the visible range. In those ceramics Fe^{3+} ions are located both in the primary spinel phase Fe:$MgAl_2O_4$ and in the secondary phase Fe:MgO, which results in a very low determined GSA cross sections of Fe^{2+} ions in tetrahedral site symmetry [49]. Recently, first GCs based on Fe^{2+}:$ZnAl_2O_4$ [52,53] nanocrystals in zinc aluminosilicate glass system were prepared and studied. Lin *et al.* reported on the development of transparent GCs based on Fe:$(Ga_{2-x}Al_x)O_3$ nanocrystals with spinel structure in the sodium-magnesium-alumino-gallo-silicate glass system and demonstrated the proof-of-the-concept of their SA performance [54]. Though there exist studies on the iron-doped GCs of the magnesium aluminosilicate system, they aim to develop opaque GCs based of iron-doped cordierite [55-57]. The preliminary results on the development of Fe:$MgAl_2O_4$-based transparent glass-ceramics were first published in [58,59].

2. Synthesis of ceramics and glass-ceramics

2.1. Synthesis of ceramics

The magnesium aluminium spinel powder doped with Fe^{2+} ions was synthesized by the sol-gel method. Metallic magnesium and aluminum (>99% purity) and isopropyl alcohol (99.9% purity) were used as starting materials. Mg and Al metals (31 and 69 wt%, respectively, which corresponds to a molar ratio of 1:2) were melted at 600 °C in an atmosphere of nitrogen. The alloy was crushed, mixed with 0.1 wt% of $SnCl_2$ and 0.2 wt% of NH_4Cl, which are the catalysts for the dissolution of the metals in alcohol, and heat-treated in an enclosed stainless steel vessel. $MgAl_2(OPr^i)_8$ (Pr^i stands for the isopropyl groups) was synthesized in a tube reactor at 80–150 °C by an addition of small portions of isopropyl alcohol to the granulated magnesium-aluminum alloy. After that, the final product was purified by vacuum distillation. Under synthesis conditions, other elements do not form volatile isopropylates. Thus, a single vacuum distillation of $MgAl_2(OPr^i)_8$ results in its high chemical purity and an exact ratio of 1:2 of magnesium to aluminum metals. The hydrolysis of 50 vol% solution of $MgAl_2(OPr^i)_8$ in isopropyl alcohol was conducted by using 1200 ml of isopropyl alcohol-water azeotropic mixture per 1 mol of alkoxide (hydrolysis with pure water leads to a strong agglomeration of hydroxides). The $MgAl_2(OPr^i)_8$:H_2O ratio was 1:8, which is an equimolar ratio required for complete hydrolysis. The azeotropic mixture contained iron (II) chloride ($FeCl_2$) as a source of iron ions. The addition of LiF (the sintering aid) was carried out as follows. 72 ml of suspension prepared by interaction of $LiNO_3{\cdot}3H_2O$ and NH_4F aqueous solutions was added to 1200 ml of Pr^iOH–H_2O azeotrope and further added into 1 mol of $MgAl_2(OPr^i)_8$ under stirring. After hydrolysis, the suspensions were cooled down to room temperature (RT) in air. Obtained suspensions were dried at 150 °C under ~1 kPa pressure followed by calcination in air at 750 °C for 3 h. Resulted spinel powders contained 0.1 mol% Fe and about 1.5 wt% of LiF.

To obtain Fe^{2+}:$MgAl_2O_4$ optical ceramics, the synthesized powders were pre-shaped, loaded into a graphite mold and heated from the RT up to 1600 °C with a heating rate of ~7.5 °C/min and held for 6 h before cooling down. The load was applied at a temperature of 800 °C and then increased up to ~50 MPa in 30 min. The pressure was released before free cooling of the furnace. The transparent ceramic disks were polished to laser-grade quality on both surfaces using a diamond suspension. The disk had dimensions of Ø13 × 2.8 mm (diameter × thickness) and a weak grey coloration due to the iron doping, see Fig. 1.

For comparison, undoped $MgAl_2O_4$ ceramic was prepared using a similar approach. The ceramic disk (Ø13 × 2.0 mm) was transparent and colorless, Fig. 1.

2.2. Synthesis of glass-ceramics

The glass with a composition of 20 MgO, 20 Al_2O_3, 60 SiO_2 (mol%) was nucleated by 10 mol% TiO_2 [60,61] and doped with 0.1 mol% FeO both added above 100% of the base glass composition. The raw materials were reagent grade. The batch for producing 400 g of glass was melted in a crucible made of quartz ceramics at 1550 °C for 3 h with stirring. The glass was poured onto a cold metal plate and annealed at 640 °C.

The transparent pale-yellow glass, Fig. 2, was subjected to double-stage secondary heat-treatments. The first stage was at 750 °C for 6 h and the temperature of the second stage ranged from 800 to 1100 °C with the same holding time of 6 h. As a result, transparent GCs were synthesized. Their color changed with the heat-treatment temperature from the pale yellow to the deep gray-brown (Fig. 2).

3. Experimental

3.1. Characterization of ceramics

The X-ray powder diffraction (XRD) patterns were measured with a Shimadzu XRD-6000 diffractometer, Cu Kα radiation with a Ni filter. The spinel lattice parameter *a* was determined by the Rietveld refinement. Morphology of the fracture surface of ceramics was characterized by scanning electron microscopy (SEM) using a MERLIN SEM microscope (Carl Zeiss). The SEM images were analyzed with the ImageJ software.

The RT Raman spectra were measured with the Renishaw inVia confocal Raman microscope using a Leica x50 objective (N.A. = 0.75). The excitation wavelength λ_{exc} was 514 nm (Ar^+ laser line).

The RT transmission spectra in the visible to near-IR and in the mid-IR were measured using a Shimadzu UV-3600 spectrophotometer and a FTIR spectrometer Bruker Tensor 27, respectively.

3.2. Characterization of glass-ceramics

The density of the initial glass and GCs was measured by the Archimedes method with toluene. The experimental error was about 0.0005 g/cm^3.

The XRD patterns were recorded using a Shimadzu XRD-6000 diffractometer with Cu Kα radiation and a Ni filter. The mean crystal size, D_{XRD}, was estimated from broadening of the diffraction peaks according to the Scherrer's equation:

$$D_{XRD} = \frac{K\lambda}{\Delta(2\theta)\cdot\cos\theta}, \quad (1)$$

where λ is the wavelength of the X-ray radiation (1.5406 Å), θ is the diffraction angle, $\Delta(2\theta)$ is the width of the peak at half of its maximum and K is the constant assumed to be 1 [62]. The error for the crystal size estimation is ~5%. The size of spinel crystals was determined using the diffraction peak with the Miller's indices (*hkl*) = (440) at $2\theta \approx 65.5°$. The size of crystals of magnesium aluminotitanate (MAT) $x\mathrm{MgTi_2O_5}y\mathrm{Al_2TiO_5}$ solid solution (ss) with a pseudobrukite structure [60,61] was determined for the (110) diffraction peak at $2\theta \approx 25.7°$. The spinel lattice parameter a was determined using the same diffraction peak with the Miller's indices (*hkl*) = (440) at $2\theta \approx 65.5°$ according to the equation:

$$a = d_{hkl}\sqrt{h^2 + k^2 + l^2} \qquad (2)$$

For differential scanning calorimetry (DSC), bulk samples of about 20 mg in weight were used. A simultaneous thermal analyzer NETZSCH STA 449 F3 Jupiter with a dynamic flow atmosphere of Ar was employed. The temperature range was RT - 1250 °C. The heating rate was 10 °C/min. The samples were the initial glass and the glass heat-treated at the nucleation stage of 750 °C for 6 h. To assign the exothermal DSC peaks to certain crystalline phases, bulk samples of about 80 mg in weight were heated in the DSC furnace with the same heating rate of 10 °C/min up to a temperature of the certain exothermal peak appearence, cooled down to RT and subjected to powder XRD analysis.

The microstructure of the initial glass and GCs was studied by transmission electron microscopy (TEM) with the JEOL TEM-1011 microscope (100 kV acceleration voltage, 0.4 nm point resolution). The samples were finely powdered and dispersed in ethanol. The obtained solution was dropped on a TEM grid which was dried for ~30 min. The TEM images were analyzed with the ImageJ software.

The Raman spectra of the initial glass and GCs were recorded with the same confocal Raman microscope as that used for studying the ceramics. For the measurment in the frequency range of 100-1200 cm^{-1}, an edge filter was used. The Raman spectra in the frequency range of 5-350 cm^{-1} were measured with a notch-filter. The spatial resolution was about 2 cm^{-1}.

The absorption spectra of the initial glass and GCs were recorded on a Shimadzu UV-3600 spectrophotometer. Double-sided polished samples (1.0 mm thick) were used. The luminescence spectra were measured using the confocal Raman microscope with λ_{exc} = 488 nm (Ar$^+$ laser line).

4. Transparent ceramics

4.1. Structure

The phase purity and the structure of ceramics were confirmed by XRD, see Fig. 3(a). $\mathrm{MgAl_2O_4}$ and Fe:$\mathrm{MgAl_2O_4}$ are cubic (sp. gr. O^7_h – $Fd\bar{3}m$, No. 227). The lattice constants of both spinels are similar, a = 8.083±0.003 Å (for the Fe:$\mathrm{MgAl_2O_4}$ spinel) and 8.088±0.003 Å (for the undoped $\mathrm{MgAl_2O_4}$ one). Quite similar lattice constants a = 8.086±0.002 Å and 8.087±0.002 Å and were reported in [50] for $\mathrm{MgAl_2O_4}$ doped with 0.1 and 1wt% $\mathrm{Fe_3O_4}$, respectively. The lattice parameter in Fe:$\mathrm{MgAl_2O_4}$ ceramic is slightly larger than that for the initial powder (a = 8.063 Å [34]), which is most likely due to the presence of a sintering aid of lithium fluoride in the powder that can enter the spinel structure [63]. During hot-pressing, the sintering aid evaporates and the fluorine and lithium ions are replaced by larger ions of oxygen and magnesium or aluminum, respectively.

No traces of any impurity phase were found. Figure 3(a) shows that the intensities of the peaks with the Miller' indices (422) and (533) in the XRD pattern of the Fe:$MgAl_2O_4$ ceramics increase as compared with the standard values (see ICSD card No. 82-2424 [64]) and with those of the $MgAl_2O_4$ ceramics. The changes in the peak intensity indicate the presence of a disordered spinel phase in the sample [65-67] caused by the iron entering the spinel crystals.

Let us shortly discuss the structure of spinels. Their chemical formula is AB_2O_4. Each unit cell contains 32 anions (O^{2-}) in a face-centered cubic packing. In the oxygen lattice, the cations (A^{2+} and B^{3+}) have 32 O_h and 64 T_d interstitial sites per unit cell. For a normal spinel, $^{IV}[A]^{VI}[B]_2O_4$, 1/8 of the tetrahedral sites are occupied by the A^{2+} cations and 1/2 of the octahedral ones are occupied by the B^{3+} cations. Here the superscripts are the coordination numbers (C.N. = IV and VI for the T_d and O_h sites, respectively). Typically, spinels demonstrate a certain degree of cation disorder. It is described by the so-called inversion parameter δ - a fraction of trivalent cations in the T_d sites (or, equivalently, a fraction of A^{2+} cations in the O_h sites). Thus, a general formula for spinels is $^{IV}[A_{1-\delta}B_\delta]^{VI}[B_{2-\delta}A_\delta]O_4$ ($\delta = 0$ and 1 correspond to a normal / inverse spinel, respectively) [68]. Note that as we mentioned before, there exists Fe-based normal spinel with $\delta \approx 0$ ($FeAl_2O_4$, hercynite) [69].

The Fe^{2+} ions are expected to replace the Mg^{2+} ones in T_d sites owing to the closeness of their ionic radii (R_{Fe} = 0.63 Å and R_{Mg} = 0.57 Å for IV-fold oxygen coordination [70]). The Fe^{2+} doping can also induce an additional cation disorder leading to appearance of both Fe^{2+} and Mg^{2+} ions in O_h sites. Andreozzi *et al.* had shown that compared with Fe^{2+}, Mg^{2+} has some preference in substituting for octahedral Al^{3+}, and that in the $MgAl_2O_4$ – $FeAl_2O_4$ isostructural series of solid solutions, the fraction of Fe^{2+} ions in O_h sites increases with the Fe content while it is near zero for low iron doping (as in our case) [17].

The morphology of the fracture surface was characterized by scanning electron microscopy (SEM), Fig. 4(a). The grain boundaries are clean and there is no secondary phase at the boundaries. This is in agreement with the XRD finding of the absence of any secondary crystal phase (Fig. 3). Due to low-defect grain boundaries, the bonds between the grains have strength comparable to that in the grain volume so that the inter- and intragranular fracture mechanisms compete in ceramics. Usually, when using sintering aid, it tends to accumulate at the grain boundaries, which weakens the bonds between the grains compared to the grain volume. This leads to the intergranular destruction of such ceramics [34]. In our case, the relatively small initial LiF content of 1.5 wt% and the long exposure time at the hot pressing temperature made it possible to completely remove the sintering aid. Another important factor for the absence of impurities at the grain boundaries may be the initially high chemical purity of the powders, achieved by vacuum distillation of the precursor. The ceramic is also almost pore-free. Low porosity and *the absence of secondary phases* make it possible to achieve high optical quality of ceramics (see below). The average grain size is about 50 μm (as determined by analyzing more than 100 grains), see Fig. 4(b). The grain size was obtained by multiplying the measured lengths by a shape factor of 1.2.

4.2. Raman spectra

Vibronic properties of ceramics were studied by Raman spectroscopy, Fig. 5. According to [63], the following vibrational modes are characteristic of the spinel structure:

$\Gamma = A_{1g}(R) + E_g(R) + 3T_{2g}(R) + 4T_{1u}(IR) + T_{1g} + 2T_{2u} + 2A_{2u} + 2E_u$.

Among these modes, the Raman-active ones are A_{1g}, E_g, and T_{2g}, while T_{1u} is IR-active. The oriented $MgAl_2O_4$ spinel single crystal has the following vibrational frequencies: 311 cm^{-1} (T_{2g}) – lattice, 410 cm^{-1} (E_g), 492 cm^{-1} (T_{2g}) – both bending, 671 cm^{-1} (T_{2g}) - asymmetric stretching, 772 cm^{-1} (A_{1g}) - symmetric stretching [71].

The same vibrations at ~195, 251, 303, 405, 496, 667, 721 and 764 cm^{-1} are found in the Raman spectra of Fe-doped and undoped ceramics. The Raman bands at 303, 405, 496, 667 and 764 cm^{-1} are close in positions to the data for the $MgAl_2O_4$ spinel single crystal [71]. Although the Raman spectra of two ceramics are rather similar, the spectrum of the iron-doped spinel is more complex: the band at 405 cm^{-1} is more broad, asymmetric and intense, the bands at 496 and 721 cm^{-1} are more pronounced, and there are also bands at 583 and above 800 cm^{-1} that are hardly seen in the spectrum of the undoped spinel. The appearance of the band at 721 cm^{-1} and a low-frequency shoulder on the intense band at 405 cm^{-1} are typical features of synthetic spinel [72]. The band at 721 cm^{-1} is assigned to symmetric Al-O stretching vibration of AlO_4 groups created by redistribution of some Al^{3+} ions from octahedral to tetrahedral sites and evidences a certain disorder of the spinel structure, while the low-frequency shoulder of the 405-cm^{-1} band appears to be the bending mode for Al ions in tetrahedral sites [73,74]. Apparently, the bands at 205 and 251 cm^{-1}, in the similar manner as the band at 300 cm^{-1}, can be attributed to the external lattice vibrations in polycrystalline ceramics.

Raman spectroscopy was successfully used to study cation disorder in spinels. It has been suggested [74] that most of extra features in Raman spectra of spinels are related to cation disordering. We speculate that appearance of additional bands in the spectrum of the Fe-doped spinel at 583 and at above 800 cm^{-1} can also stand for a certain degree of its disorder caused by Fe^{2+} doping. Thus, we can conclude that the comparison of Raman spectra of Fe-doped and undoped spinel proves the increase of the cation disorder in spinel with an addition of iron ions, which is in accordance with the XRD findings. It is also known [74] that the complex Raman spectrum of iron-doped spinel can be affected not only by the substitution $Fe^{2+} \rightarrow Mg^{2+}$ and the cation disorder, but also by the entrance of small amounts of Fe^{3+} in the spinel structure. It is not surprising that the addition of 0.1% Fe does not affect the position of the Raman peaks. According to [75], while the substitution $Fe^{2+} \rightarrow Mg^{2+}$ proceeds along the $MgAl_2O_4$ – $FeAl_2O_4$ series, no change in the wavenumber of the E_g, T_{2g}, and A_{1g} modes is observed up to the Fe^{2+} content of ~20%.

In agreement with the XRD data, no signals attributed to impurities or secondary phases are identified in the Raman spectra of both spinels.

4.3. Optical absorption

The in-line transmission spectrum of the polished $Fe:MgAl_2O_4$ ceramic disk (recalculated for a reference thickness of 1.0 mm) is presented in Fig. 6(a) and compared with that for the undoped $MgAl_2O_4$ ceramic. The transparency range for both samples is similar, 0.2–6.0

μm. $MgAl_2O_4$ possesses a large direct bandgap of $E_g = 7.8$ eV (the corresponding wavelength of the UV absorption edge λ_{UV} ~0.16 μm) [76]. For the undoped ceramic, the in-line (small-signal) transmission T at the wavelength of ~1 μm is 82.2% (compare with the theoretical value set by the Fresnel losses, $T_0 = 87.0\%$ for a refractive index $n = 1.704$ [9]). For the Fe-doped ceramics at the same wavelength of ~1 μm, T is reduced to a value of 74.4%.

In the spectrum of the Fe-doped ceramics, there is an intense absorption band in the near-mid-IR, spanning from ~1.2 to 3.7 μm with the local maxima at 1.90 and 2.82 μm. It is assigned to the absorption of Fe^{2+} ions in T_d sites in spinel. The electronic configuration of Fe^{2+} ion is [Ar]3d^6. Thus, the energy-level scheme for the Fe^{2+} ion in the tetrahedral ligand field is equivalent to a 3d$^{(10-n)}$ = 3d^4 ion in the octahedral ligand field. The ground state of the free ion is the ^5D one and it is split in the tetrahedral ligand field into the ^5E and $^5T_2$ levels separated by an energy Δ = 10Dq. The spin-allowed transitions between these levels determine the intense absorption and emission bands of $^{IV}Fe^{2+}$ ions. Indeed, an intense absorption band in the NIR range centered at ~5000 cm^{-1} has been widely attributed to the spin-allowed electronic d–d transition ($^5E \rightarrow {}^5T_2$) in tetrahedrally coordinated Fe^{2+} [18-22,77-80]. The band is characterized by a distinct shoulder at ~3500 cm^{-1}, due to the dynamic Jahn–Teller effect for tetrahedral Fe^{2+} ions in the spinel structure [21,79]. Our data are in agreement with Gaffney [18] who reported on the following energies of this transition in absorption: 3600 and 4900 cm^{-1} (λ = 2.78 and 2.04 μm). For tetrahedrally coordinated Fe^{2+} ions, there also exist higher-lying triplet states (^3H, ^3P, ^3F, ^3G), however, the transitions to these states are spin-forbidden and thus very weak.

Apart from $^{IV}Fe^{2+}$ ions, as pointed out above, there can exist $^{VI}Fe^{2+}$ ones in the disordered spinel structure. In general, because the O_h site has a center of symmetry, the transition intensities for transition metal ions located in the ligand field of octahedral symmetry are by several orders of magnitude weaker than those in the field of tetrahedral symmetry. Absorption of $^{VI}Fe^{2+}$ ions was observed before mainly in highly doped samples. Gaffney [18] assigned transitions at 9500 and 10800 cm^{-1} (λ = 1.05 and 0.93 μm, respectively) to the spin-allowed $^5T_2 \rightarrow {}^5E$ (^5D) absorption transition in the octahedral (O_h) field. No absorption at these wavelengths is found in the ceramic sample under study. Dickson *et al.* predicted the molar extinction coefficient ε for this absorption band to be 0.51 l·mol^{-1}·cm^{-1} [81] (compare with the value of 59 l·mol^{-1}·cm^{-1} for the $^{IV}Fe^{2+}$ absorption [23]. According to [17], in spinel, Fe^{2+} shows a marked preference for tetrahedral coordination with respect to Mg^{2+}, thus, the absence of absorption caused by the $^{VI}Fe^{2+}$ ions is not surprising.

Another possibility for Fe ions to be accommodated in the spinel lattice is to do it in the form of Fe^{3+} (in the O_h sites, by replacing Al^{3+} ions). The corresponding ionic radii are R_{Fe} = 0.645 Å, high-spin, and R_{Al} = 0.535 Å for VI-fold oxygen coordination [70]. The presence of Fe^{3+} ions in oxide crystals can be manifested by absorption transitions of both isolated Fe^{3+} ions (d-d transition) and Fe^{2+}-Fe^{3+} ion pairs (intervalence charge transfer, IV CT, transition) [23]. The characteristic transitions are at 21700 and 21300 cm^{-1} (λ = 0.46 and 0.47 μm, respectively) – for the $^6A_{1g} \rightarrow {}^4A_{1g} + {}^4E_g(^4G)$ transitions for the isolated $^{VI}Fe^{2+}$ ions and ion pairs, respectively [23]. None of these bands were observed in the studied ceramics. This finding is in accordance with [82], which states the iron atoms at low concentration are diluted in the system and located far from each other. However, we cannot rule out that we noticed no trace of Fe^{3+} ions in the O_h sites due to the low intensity of their absorption bands.

In the previous works [49-51,83-85], the presence of Fe^{3+} was detected by measuring the visible luminescence spectra of iron-doped samples revealing emissions centered at ~0.51, 0.62 and 0.72 μm and originated from the ^4G excited states. The emission spectrum for our ceramic sample is shown in Fig. 7. In fact, Fig. 7 demonstrates a typical red fluorescence spectrum of $MgAl_2O_4:Cr^{3+}$ [86,87]. The red emission at 687 nm is assigned to the $^2E_g \rightarrow {}^4A_{2g}$ spin-forbidden transition of Cr^{3+} ions located at the Al^{3+} sites [87]. A very week luminescence of Fe^{3+} ions can probably reveal itself by the broad band of low intensity in the range of 540 – 650 nm and partly be concealed in the luminescence spectrum of the Cr^{3+} ion. The absorption spectrum of $MgAl_2O_4:Cr^{3+}$ consists of two broad bands in the visible spectral range, at ~390 nm (the $^4A_{2g} \rightarrow {}^4T_{1g}$ transition) and at ~540 nm (the $^4A_{2g} \rightarrow {}^4T_{2g}$ transition). We did not observe the characteristic absorption bands of Cr^{3+} ion in the absorption spectrum of our $Fe:MgAl_2O_4$ ceramic sample (see Fig. 6). Therefore, the concentration of this uncontrolled impurity ion in the ceramic sample is extremely low. According to the study of Bubnova and Solomonov [51], the characteristic luminescence bands of Cr^{3+} ions are not observed in spinels containing Fe^{3+} ions due to the quenching originating from the nonradiative energy transfer between chromium excited-states and the lower-lying levels of iron ions. Consequently, the fact that the luminescence spectrum of our $Fe:MgAl_2O_4$ spinel ceramic presents the luminescence of Cr^{3+} ions is an evidence of the absence or an extremely low content of Fe^{3+} ions in the material.

In the UV part of the absorption spectrum of the $Fe:MgAl_2O_4$ ceramic, there is an absorption band centered at 0.26 μm. This band is too intense for the spin-forbidden $^{IV}Fe^{2+}$ transitions. It can originate from the oxygen to Fe^{2+} and probably to Fe^{3+} charge transfer (oxide to metal charge transfer, OMCT). The corresponding absorption peaks are located at about 250 nm and 210 nm, respectively [88]. This suggestion is in accordance with Gaffney's finding [18] that Fe^{3+} impurities do not contribute directly to the visible spectra of most of these minerals, with the exception that Fe^{3+} probably contributes to the intense ultraviolet absorption.

The ground-state absorption (GSA) cross section, σ_{GSA}, for the $^5E \rightarrow {}^5T_2$ (^5D) transition of Fe^{2+} in $MgAl_2O_4$ was calculated assuming that all the iron ions in the ceramic are optically active and there is no contribution of $^{VI}Fe^{2+}$ and Fe^{3+} species. The results are shown in Fig. 6(b). Here, we use the nominal iron concentration $N_{Fe} = 1.516 \times 10^{19}$ cm^{-3} (as calculated for the theoretical spinel density $\rho = 3.578$ g/cm^3). The maximum σ_{GSA} is calculated to be 0.28×10^{-18} cm^2 at 1.90 μm.

For comparison, in Fig. 6(b), we also plotted the GSA cross section spectra for Fe^{2+} ions in ZnS and ZnSe crystals (measured in this work using samples fabricated at G.G. Devyatykh Institute of Chemistry of High-Purity Substances, RAS). The absorption band in the Fe-doped spinel is blue-shifted by ~1 μm as compared to that for the Fe:ZnSe material while showing a very similar shape. The value of σ_{GSA} for the $Fe:MgAl_2O_4$ spinel is reduced by a factor of ~3 (compare with $\sigma_{GSA} = 0.97 \times 10^{-18}$ cm^2 at 3.11 μm for the Fe:ZnSe sample). We believe that this difference mainly originates from the host matrix. In part, it may also originate from the presence of traces of $^{VI}Fe^{2+}$ and Fe^{3+} species that do not contribute to the absorption at 1.90 μm). Another possible mechanism responsible for decreasing the concentration of optically active iron ions in the ceramic compared to its initial concentration in the powder may be reduction of the Fe^{2+} ions to the metallic state due to the presence of residual hydrocarbons and carbon monoxide from the graphite equipment of the hot press. However, one of the features of LiF as a sintering additive is effective removal of carbon-containing impurities from ceramics at the open porosity stage. This prevents intensive reduction of Fe^{2+} ions. We believe that the concentration of optically active iron is close to its initial concentration in the powder.

It is worth mentioning that the described reduction mechanism can be partly responsible for the appearance of optically inactive iron in [47], as supported by much lower σ_{GSA} of only $(1.66\pm0.14)\times10^{-20}$ cm^2 reported in that work. Its indication is the dark coloration of samples in [47]. Another reason for such a low σ_{GSA} is the presence of $^{\mathrm{VI}}Fe^{2+}$ in this ceramics, as manifested by intense absorption band at ~1 μm [47].

5. Transparent glass-ceramics

5.1. Structure

The density variation for the initial glass with the heat-treatment temperature is shown in Fig. 8. It demonstrates a complex behavior typical for density variation of spinel based GCs [29]. The density of the initial glass is 2.6120 g/cm^3. After the heat-treatment at 750 °C, the density slightly increases to 2.6151 g/cm^3, and after two-stage heat-treatments in the temperature range of 800–900 °C it rapidly increases up to 2.7147 g/cm^3. The GCs prepared at the second stage in the temperature range of 950–1000 °C have lower densities (the GC prepared at 1000 °C has a density of 2.6809 g/cm^3). The density of GC prepared at 1050 °C is higher, namely 2.7148 g/cm^3.

The DSC curves for the initial glass and the glass heat-treated at 750 °C for 6 h are drastically different, Fig. 9. Though the glass transition temperature, T_{g}, is about 740 °C for both glasses, in the temperature range of 800–1000 °C they behave differently. For the initial glass, there is an intense narrow peak with the crystallization onset temperature (T_{on}) of 880 °C and the maximum crystallization temperature of 909 °C. This peak demonstrates an asymmetric wing from the low-temperature side. For the glass heat-treated at 750 °C for 6 h, there are three rather broad exothermal peaks with the crystallization onset temperatures of 795, 934 and 1085 °C and maximum crystallization temperatures of about 859, 973 and 1160 °C, respectively, Fig. 10. It was challenging to determine the origin of these peaks for both DSC curves. That is why, after the crystallization onset temperatures were determined, the samples of the initial glass and the glass preliminary heat-treated at 750 °C for 6 h, both about 80 mg in weight, were heated in the DSC instrument up to the crystallization onset temperatures.

According to the XRD data, Fig. 10(a), in the DSC curve of the initial glass, the first exothermal peak is associated with crystallization of the magnesium aluminotitanate (MAT) solid solution (ss) (probably, its crystallization corresponds to the low-temperature wing of the exothermal peak) and of the magnesium aluminosilicate with a quartz-like structure. The sample heat-treated up to the temperature of the second exothermic peak (1160 °C) had a rich phase composition of the MAT ss, magnesium aluminosilicate with a quartz-like structure, sapphirine, rutile, traces of indialite, a high-temperature modification of cordierite, and traces of mullite.

The XRD patterns of GCs prepared from the glass heat-treated at 750 °C for 6 h showed that the first crystallization peak is due to formation of spinel and traces of MAT ss. The sample heated up to 970 °C contained crystals of both MAT ss and spinel, while after heating up to 1150 °C, the sample contained the MAT ss and sapphirine crystals, as shown in Fig. 10(b).

The XRD patterns of the initial glass and GCs obtained by secondary heat treatments in the temperature range from 750 to 1050 °C are shown in Fig. 11. The initial glass and the glass heat-treated at the nucleation stage (at 750 °C for 6 h) are X-ray amorphous. The color change (Fig. 2) and density increase (Fig. 8) after the heat treatment at 750 °C suggest amorphous phase separation of the initial glass. This assumption will be confirmed below using TEM, Raman and optical spectroscopy data.

The XRD patterns show that after two-stage heat-treatments with the second stage in the temperature range of 800–1000 °C, two crystalline phases, MAT ss and spinel, crystallize and grow. With increasing the heat-treatment temperature, intensities of the peaks on the XRD patterns increase, and the intensity of the amorphous halo decreases. It means that the crystallinity fraction in GCs increases with the heat-treatment temperature. When the temperature rises from 800 to 1000 °C, the spinel mean crystal size grows from 37 to 74 Å, while the size of MAT crystals increases from 64 to 206 Å (see Table 1). The spinel unit cell parameter *a* increases with the heat-treatment temperature from 8.002 Å (at 800 °C) to 8.079 Å (at 1000 °C). As it was mentioned before, there exists an infinite solid solution in the $MgAl_2O_4$–$FeAl_2O_4$ system with the unit cell parameter *a* variation from 8.0855 to 8.1646 Å [17]. Therefore, one would expect larger spinel unit cell parameter in GCs. The low value of the parameter *a* implies that the composition of the spinel under study is enriched in alumina, which agrees with our previous observations [61]. An increase of the lattice constant of spinel under study with the heat-treatment temperature could be explained mainly by the decrease of the excess of aluminum in the spinel composition and additionally by an increase of the order in the spinel structure [29].

As soon as the crystals of spinel and MAT ss are formed at 800 °C, there is a shift of the amorphous halo position to smaller angles, which manifests a change in the composition of the residual glass. With increasing the heat-treatment temperature, the position of the amorphous halo becomes close to that of the vitreous silica, as the residual glass composition becomes more and more silica enriched.

In the temperature range of 1050–1100 °C, sapphirine, the solid solution with a composition lying between $2MgO\cdot 2Al_2O_3\cdot 1SiO_2$ and $7MgO\cdot 9Al_2O_3\cdot 3SiO_2$ [89] is also formed. After the two-stage heat treatment with the second hold at 1050 °C, the GC is transparent, while after the heat treatment at 1100 °C, it is translucent. It is the first time to our knowledge that transparent GC based on sapphirine are prepared (see Fig. 2 and Fig. 11, 1050 °C).

A typical TEM image of the initial glass, Fig. 12(a), shows amorphous phase separation in accordance with our previous studies [61]. Note that the XRD pattern of the sample indicates the lack of any crystalline phase. The phase separation develops after the nucleation stage of the heat treatment at 750 °C, Fig. 12(b). The phase separated regions (mean size: D_{TEM} ~3.3 nm) are still X-ray amorphous. In the TEM image of the GC sample obtained at 950 °C, nanocrystals (D_{TEM} ~6.4 nm) with a rectangular and elongated shape are observed. They are most probably the spinel nanocrystals. Indeed, the corresponding D_{XRD} = 7.4 nm (spinel) and 20.6 nm (MAT ss), see Table 1.

The complex character of the density variation with the heat-treatment temperature, when the density first increases and then slightly decreases, cf. Fig. 8, is related to a complex structure of the GCs described above and, in particular, to different densities of the spinel and MAT solid solutions and the amorphous phase with composition close to the vitreous silica, whose ratio changes with temperature. In addition, the composition of solid solutions also change in a complex way. The density increase is observed for the GC prepared at 1050 °C and containing sapphirine nanocrystals and increased fraction of MAT ss, Fig. 10. It could not be associated with the crystallization of sapphirine as the densities of spinel (~3.58 g/cm^3 [9]) and sapphirine (3.40-3.58 g/cm^3, depending on its composition [90]) are similar. Thus, this effect is probably connected with increased fraction of the MAT ss containing Fe ions (see below). Note that the armalcolite density is ~4.94 g/cm^3 [91].

5.2. Raman spectra

The Raman spectra of the initial and heat-treated glasses demonstrate the structural evolution of the material, see Fig. 13(a). The spectrum of the initial glass contains two broad bands, one with a maximum at 478 cm^{-1}, and another of a complex shape with several maxima at 802, 920 and 1025 cm^{-1}. The bands at 478, 802 and 1025 cm^{-1} are attributed to vibrations of tetrahedra of the aluminosilicate network. The very intense band at 920 cm^{-1} is attributed to vibrations of the [TiO_4] tetrahedra incorporated into the aluminosilicate network [60].

After the heat-treatment of the glass at 750 °C for 6 h (the nucleation stage), its Raman spectrum changes. The broad band at 478 cm^{-1} shifts to 466 cm^{-1} and the band intensities in the high-frequency region are redistributed: the band at 920 cm^{-1} shifts to 910 cm^{-1} and attenuates, and the band at 800 cm^{-1} shifts to 814 cm^{-1} and enhances. These changes are caused by development of the phase separation of the glass: the magnesium aluminotitanate amorphous phase (with a characteristic band at 810 cm^{-1}) and the phase enriched in magnesia and alumina are formed in the residual silica-rich phase (the manifestation of the latter phase is the shift of the band characteristic for the glass network from 478 cm^{-1} to 466 cm^{-1}). Thus, the so-called three-phase immiscibility [61] is developed. The high intensity of the 814 cm^{-1} band can be explained by the superposition of vibrations of the [SiO_4] tetrahedra and those of the Ti–O bonds in [$TiO]_5$ and in [$TiO]_6$ polyhedrons in the amorphous magnesium aluminotitanate phase [60].

The Raman spectra of GCs prepared by two-stage heat treatments are different from those previously discussed. In the Raman spectrum of GC prepared at 750 °C (the first stage) and at 800 °C (the second one), there is a broad band at 450 cm^{-1} (note that for pure SiO_2, it is located at 440 cm^{-1}), an intense band of 810 cm^{-1} with an inflection at 915 cm^{-1}, and a number of weak bands at 148, 285 and ~690 cm^{-1}. These changes indicate further phase separation of the glass and beginning of the MAT ss crystallization. The bands at 148, 285, 603 and ~690 cm^{-1} and the intense band at 810 cm^{-1} which is superimposed on the band of the amorphous magnesium aluminotitanate phase, can be attributed to the spectrum of the MAT ss with a rather high alumina content [60]. After further increasing the temperature of the second stage of the heat treatment to 850 °C, the bands at 219, 272, 385, ~487, ~690 and 802 cm^{-1} appear in the Raman spectrum that can be attributed to the MAT ss crystals. Note that the weakest bands in the frequency range of 334-496 cm^{-1} are superimposed on the band at ~450 cm^{-1} originating from the residual glass phase, and it is difficult to determine their position more precisely. With a successive increase in the heat-treatment temperature of the glass from 900 to 1000 °C, almost all bands of the MAT ss are observed in the Raman spectrum. They are located at 167, 209, 261, ~375, ~487, 668, 789 and ~900 cm^{-1} (a weak wing of the intense band near 800 cm^{-1}), and their positions slightly vary reflecting the variation of the ratio of magnesium and aluminum in the MAT ss at the particular temperature. After the heat-treatment with the second stage at 1050 °C, the bands are shifted to higher frequencies of 170, 215, 266, ~383, ~487, 681, and 797 cm^{-1}, which indicates an additional enrichment of the solid solution with alumina (note that the weak band at 456 cm^{-1} does not belong to the spectrum of the MAT ss).

We speculate that iron ions Fe^{2+} can enter the crystals of MAT ss. There exist a mineral armalcolite, which has a general chemical formula of $(Mg^{2+},Fe^{2+})Ti_2O_5$. Together with MAT, it belongs to the pseudobrookite group. The Raman spectrum of armalcolite [92] is similar to that of the MAT ss. Thus, one can expect that entering the Fe^{2+} ions into the structure of MAT ss should not disturb the structure and will not cause a serious change of the Raman spectrum.

After the two-stage heat treatments with a second stage at 950–1000 °C, a weak and then more distinct maximum appears at 409 cm^{-1}, which corresponds to the most intense band of spinel [70]. Note that, apparently, due to the large difference in the scattering cross sections for crystals of MAT ss and spinel, in the Raman spectra of the heat-treated glass the bands of MAT ss are always the most intense, and spinel is hard to be observed.

After increasing the heat-treatment temperature to 1050 °C, according to XRD data, Fig. 11, sapphirine crystals are detected in addition to spinel and MAT ss. We tried to find any signs of sapphirine in this Raman spectrum. In the RRUFF database [93], there are Raman spectra of several sapphirine minerals with peak positions at about 220, 410, 495, 565, 685, 750, 825, 915 and 985 cm^{-1}. Two of these bands are the most intense, i.e., at 565 and 685 cm^{-1}, of which the second is about 1.6 times more intense than the first. Figure 13(a) shows that the position of the most intense Raman band of sapphirine at 685 cm^{-1} nearly coincides with the position of the band of MAT ss at 681 cm^{-1}. A very weak trace of the second most intense sapphirine band is found at 562 cm^{-1}. The trace of the band at ~ 409 cm^{-1} is the superposition of spinel and sapphirine bands. The sapphirine band of intermediate intensity at 915 cm^{-1} is superimposed on the high-frequency tail of the intense band of the MAT ss at 795 cm^{-1}. Thus, there is no significant impact of sapphirine crystallization on the Raman spectrum of GC since intensities of all the bands do not change noticeably when comparing the spectrum of the GC prepared at 1000 °C with that of the GC prepared at 1050 °C.

5.3. Low-frequency Raman spectra

The Raman spectra of the initial glass and the glass subjected to heat-treatment at the nucleation stage (at 750 °C for 6 h) did not show any low-frequency band. This band appears after two-stage heat-treatments and its position shifts to lower frequencies with increasing the heat-treatment temperature, Fig. 13(b).

There is a correlation between the position of the low-frequency Raman band and the size of inhomogeneous regions [94,95]:

$$\nu^{\mathrm{s}}_{02} = \frac{\xi^{\mathrm{s}}_{02} \upsilon_l}{2\pi R \cdot c}, \tag{3}$$

where ν^{s}_{02} is the frequency of the spheroidal vibration mode corresponding to the low-frequency peak, which is mostly active in Raman scattering, ξ^{s}_{02} is the phenomenological coefficient depending on the relation between the transversal, υ_t, and longitudinal, υ_l, velocities of sound in the inhomogeneous regions and on the particle interface, R is the radius of the inhomogeneous region (assuming its nearly-spherical shape) and c is the speed of light. The mean size (D_{Raman}) of inhomogeneous regions is [96]:

$$D_{\mathrm{Raman}} \approx \frac{0.8\upsilon_l}{c\,\nu^{\mathrm{s}}_{02}}. \tag{4}$$

Our earlier study of phase separation in heat-treated magnesium aluminosilicate glasses nucleated by TiO_2 using small-angle X-ray scattering [61,97] showed that a bidispersed system of inhomogeneities is formed at the initial stages of phase separation. The sizes of the smaller regions were found to be consistent with the sizes obtained from the position of the low-frequency Raman band under an assumption that at the beginning of the process, these are amorphous silicate inhomogeneities enriched in magnesium and aluminum, in which spinel crystallizes with increasing the heat-treatment temperature. Large-size inhomogeneities, at first also of amorphous nature, form magnesium-aluminum-titanate phase, from which the MAT ss crystallizes with increasing the heat-treatment temperature.

The sound velocity for spinel crystals $\upsilon_l = 10\times10^5$ cms^{-1} [98]. When calculating the sizes of inhomogeneous regions D_{Raman} listed in Table 1, we have chosen a slightly lower sound velocity, $\upsilon_l = 8\times10^5$ cms^{-1}, since a certain amount of SiO_2 is always present in magnesium aluminate regions of inhomogeneity. For SiO_2, υ_l is less than 6×10^5 cms^{-1} [98]. The results presented in Table 1 allowed us to conclude that these regions of inhomogeneity are not completely crystallized, since the diameter of spinel crystals according to the XRD and TEM data is approximately half of that calculated from the position of the low-frequency Raman band.

5.4. Optical absorption

The absorption spectra of the initial glass and GCs are presented in Fig. 14(a-c). For the initial glass, the UV absorption edge is observed at $\lambda_{\mathrm{UV}} = 0.34$ μm. The spectrum contains a broad band in the range of 400-600 nm, a maximum of which is superimposed with the absorption edge, a weak and broad band at 0.75–1.5 μm with a peak at ~1.05 μm and a weak shoulder extending until 2.5 μm, and a broad asymmetric band in the in the range of 2.7 – 3.1 μm. The spectrum of the glass heat-treated at 750 °C for 6 h (the nucleation stage) is different from the spectrum of the initial glass mainly in the UV and visible ranges: the absorption edge is red-shifted by about 7 nm, and a broad band in the visible intensifies and becomes broader, it now spans until 700 nm.

The spectrum of the GC prepared by the two-stage heat-treatment with the second stage at 800 °C demonstrates a similar evolution: the absorption edge is further red-shifted by about 6 nm, and a broad band in the visible spectral range intensifies and becomes even broader now spanning until 900 nm.

With increasing the temperature of the heat-treatment at the second stage (850–1000 °C), the spectra of the GCs change in a different way. The slope of the UV absorption edge becomes smoother, while its position is slightly changing in the range of λ_{UV} = 0.34-0.35 μm. There is also a great raise of absorption in the visible with a maximum at ~0.55 μm and in the near IR, and an increase in intensity of the broad absorption band at 0.75–1.5 μm, Fig. 14(b). A broad band at 1.4–2.5 μm with a maximum at ~1.88 μm appears and grow with increasing the heat-treatment temperature. The mid-IR absorption is structured with two components at 2.73 and 2.92 μm, Fig. 14(c).

Finally, for the GC obtained at 1050 °C, the absorption edge experiences a notable red-shift to λ_{UV} = 0.37 μm. The absorption at ~1.88 μm decreases. Simultaneously, the absorption in the visible and at ~1.1 μm raises.

The interpretation of the absorption spectra is complicated because in the initial glass and in GCs, there are two polyvalent transition metal ions that can be responsible for light absorption, i.e., titanium and iron ones, and both ions participate in phase transformations caused by heat-treatments, which alternates their surrounding.

In general, titanium ions are found in glasses and minerals under two oxidation states of Ti^{3+} ($3d^1$) and Ti^{4+} ($3d^0$). The absorption band due to the $^2T_{2g} \rightarrow E_g$ transition of the Ti^{3+} ion in O_h site symmetry is located at about 500 – 625 nm depending on the ligand field strength and distortions of its symmetry [99,100], while the band due to the $E_g \rightarrow {}^2T_{2g}$ transition of Ti^{3+} in T_d site symmetry is located at about 1000 nm [100,101]. The O-Ti^{3+} OMCT band is predicted in the UV spectral range at about 240 nm [102]. Ti^{4+} ions do not exhibit any d-d transition while they are responsible for the O-Ti^{4+} OMCT band which is located in the UV spectral range at about 300 nm [102], as well as participate in homonuclear IV CT Ti^{4+}/Ti^{3+} and heteronuclear $Fe^{2+} + Ti^{4+} \rightarrow Fe^{3+} + Ti^{3+}$ transitions that give rise to intense absorption bands in the visible spectral range. In different minerals, IV CT Ti^{4+}/Ti^{3+} transition gives rise to a band at about 480 nm [103], 660 - 670 nm [104].

Iron ions in glasses exist under two oxidation states, ferrous, Fe^{2+} ($3d^6$) and ferric, Fe^{3+} ($3d^5$). The analysis of the absorption spectra caused by iron ions in glasses is difficult because all transitions of Fe^{3+} and Fe^{2+} ions, except of those giving rise to bands in the region of 1 and 2 μm, are spin-forbidden and therefore have weak intensities; the corresponsing bands are superimposed on very intense (especially in case of Fe^{3+} ions) IV CT (at least 10 times more intense) and OMCT (100 to 1000 more intense) bands. Moreover, Fe^{3+} and Fe^{2+} ions often coexist, they can be fourfold-, fivefold- and sixfold-coordinated, and similar forbidden bands fall into the same spectral range and overlap [101,105]. For the assignment of absorption bands in the spectra of glasses, a comparison with absorption spectra of minerals with well-established structure is employed [105], additional methods of analysis are used, i.e., high-resolution X-ray absorption near-edge structure (XANES) spectra [106] or Mössbauer spectra [100,107].

In the spectra of ferric ions in silicate glasses, the OMCT Fe^{2+} -O band is located at about 235 nm, while weak spin-forbidden bands can be found around 21500 and 23400 cm^{-1} (at 465 and 430 nm, respectively) [105] and are assigned to the Fe^{2+} spin-forbidden transitions $^5T_2(D) \rightarrow {}^3T_1(H)$ and $^5T_2(D) \rightarrow {}^3T_2(H)$, respectively. The broad bands at about 1000 and 2000 nm are attributed to the spin-allowed electronic d–d transitions $^5T_2 \rightarrow {}^5E$ and $^5E \rightarrow {}^5T_2$ for octahedrally and tetrahedrally coordinated Fe^{2+} ions, respectively [100,101].

In the spectra of ferric ions in silicate glasses, the OMCT Fe^{3+} -O band is located at about 270 nm [105] and it spans until the visible spectral range. It often even overlaps with peaks located at about 370, 380, 420, 440, and 480 nm and assigned to d-d transitions of $^{[4]}Fe^{3+}$, $^{[5]}Fe^{3+}$ and $^{[6]}Fe^{3+}$ ions [105].

Fe^{2+} -Fe^{3+} and Fe^{2+}-Ti^{4+} coordination clusters may coexist in the same structure, and give rise to homonuclear $Fe^{2+} \rightarrow Fe^{3+}$ and heteronuclear $Fe^{2+} \rightarrow Ti^{4+}$ intervalence transitions in the visible region, thereby complicating the assignment of absorption bands [104]. The Fe^{2+}-Ti^{4+} IV CT transition is believed to contribute to the UV-visible spectra of synthetic Fe-Ti silicate glasses [108]. In [100], it was found at about 450 nm contributing to the absorption edge of the glass. IV CT $Fe^{2+} \rightarrow Fe^{3+}$ transitions are observed in the range of 540 - 660 nm, as well as at around 730-770 nm [104].

The spectral changes observed upon the heat-treatments of the initial glass under study confirm that the titanium and iron ions are involved in phase transformations. The absorption edge of the initial glass is caused by the O-Ti^{4+}, O-Fe^{2+}, and O-Fe^{3+} OMCT overlapping spectral bands. According to Mysen [109], in magnesium aluminosilicate glasses, iron exists in the forms of ferrous (Fe^{2+}) and ferric (Fe^{3+}) ions with 4-, 5-, and 6-fold coordination states. The absorption band in the range of 400-600 nm is probably due to spin-forbidden d-d absorption bands of ferrous and ferric ions [105], while the weak and broad absorption band at 0.75–1.5 μm with a peak at ~1.05 μm can be associated with Fe^{2+} ions in O_h sites in the glass network. A weak shoulder extending until 2.5 μm can be connected with a minor fraction of Fe^{2+} ions in T_d sites. A broad asymmetric band in the in the range of 2.7 – 3.1 μm is caused by very intense absorption bands due to O–H vibrations of hydroxyl groups in glass.

The variation of the absorption spectrum after the heat-treatment at the nucleation stage is connected with the development of the three-phase immiscibility. Ferrous ions probably enter magnesium aluminate and magnesium aluminotitanate amorphous regions resulting in $Fe^{2+} + Ti^{4+} \rightarrow Fe^{3+} + Ti^{3+}$ IVCT transitions.

The red shift of the absorption edge and a great raise of absorption in the visible spectral range after secondary heat treatments is consistent with crystallization of spinel and MAT ss and possible entering of iron ions into these phases. Absorption spectra of iron-doped spinels are well-documented and discussed [18,20-23,77-81,110]. The broad absorption bands in the visible part of spectra of Fe-doped spinels are usually attributed to different spin-forbidden d-d transitions of Fe^{2+} and Fe^{3+} ions in the spinel ligand field [21,110], while the additional weak band at ~15000 cm^{-1} (~670 nm) can be assigned to the Fe^{2+}-Fe^{3+} exchange interaction [110]. In the spectra of GCs under study we can undoubtedly see the signs of Fe^{2+} and Fe^{3+} ions in the spinel structure, as well as IV CT transitions associated with Ti^{3+}/Ti^{4+}, Fe^{2+}/Fe^{3+} and $Fe^{2+} + Ti^{4+} \rightarrow Fe^{3+} + Ti^{3+}$. It should be noted that broad d-d absorption bands of Ti^{3+} ions in synthetic magnesium aluminate spinel are localized in the spectral region of 510 and 760 nm [111]. We cannot exclude their appearance in absorption spectra of GCs under study. An appearance and growth of the bands in the IR spectral range is due to the entry of Fe^{2+} ions into spinel nanocrystals in both the tetrahedral (predominantly) and octahedral positions. The mid-IR absorption with two components at 2.73 and 2.92 μm is developed on the basement of the broad asymmetric unstructured band of OH^- groups in the residual glass. It is interesting to note that the position of the short wavelength component of this band experiences a gradual blue-shift from 2.8 to 2.73 μm with increasing the temperature of the heat-treatment, Fig. 14(c). We connect the structuring of the absorption bands due to O–H vibrations with spinel crystallization because it is observed only in the spectra of samples containing spinel nanocrystals. Note that in synthetic spinel, the structuring of the band associated with OH groups was observed and assigned to OH groups entering the spinel structure [112,113]. However, the positions of these bands at 2985 nm (3350 cm^{-1}) and 2818 nm (3548 cm^{-1}) are different from those observed in our GCs while the reason for this discrepancy still remains unclear.

For the GC obtained at 1050 °C, a notable red-shift of the UV absorption edge reflects an increase in light scattering by relatively large sapphirine crystals. The absorption at ~1.88 μm associated with Fe^{2+} ions in T_d sites in spinel decreases. Simultaneously, the absorption in the visible and at ~1.1 μm raises. This correlates with the decrease in the amount of precipitated spinel and appearance of sapphirine. In sapphirine, Mg^{2+} ions are in sixfold coordination while Al^{3+} ions are in four- and sixfold coordinated sites [114]. Sapphirine accommodates iron ions and exhibits the substitutions Mg → Fe^{2+} (predominantly) and Al → Fe^{3+} [113] with Fe^{3+} ions assigned to tetrahedral positions [115]. Thus, upon sapphirine formation from spinel and residual highly siliceous glass, iron ions are present as the $^{VI}Fe^{2+}$ and $^{IV}Fe^{3+}$ species, which is reflected in absorption spectra.

Due to the complex distribution of iron ions over several phases, as well as the presence of iron species with different coordination and valence states, it is very difficult to make a reliable estimation of the fraction of iron ions located in spinel nanocrystals. The determination of the ground-state absorption cross-section for Fe^{2+} ions in $MgAl_2O_4$ (e.g., in an absorption saturation experiment) may facilitate such estimates.

5.4. Luminescence

The luminescence spectrum of GCs (Fig. 15) strikingly resembles that of ceramic (Fig. 7) that was assigned to impurity Cr^{3+} ions in O_h sites of spinel. This means that the evolution of the luminescence properties on the initial glass with the heat-treatment should be connected with impurity Cr^{3+} ions located in different phases. Let us discuss the spectral-luminescence properties of Cr^{3+} ions in the initial glass and in GCs. In oxide glasses, Cr^{3+} ions occupy a variety of sites with different crystal field strengths due to site variability and compositional disorder. Cr^{3+} is generally recognized as being in O_h symmetry with certain distortions [116]. According to [117], for trivalent chromium in octahedral coordination, the $^4T_{2g} \rightarrow {}^4A_{2g}$ transition is typical in the low crystal field materials with a substantial participation of the site-to-site disorder, i.e., in glasses. The Cr^{3+} luminescence in silicate glasses in low-crystal field is at ~800 nm [116,118,119]. The luminescence spectrum of the initial glass in the visible contains a weak broad band with a maximum at about 750 nm (Fig. 15). After the heat-treatment at 750 °C, the intensity of the luminescence band increases. A disproportional increase in intensity of the short-wavelength wing changes the shape of the luminescence band, while the peak position at about 750 nm does not change. After two-stage heat-treatments and with increasing the temperature at the second stage (800–1050 °C), the luminescence spectra of the GCs further change. Sharp peaks with maxima at 667, 676, 688, 698, 709, and 717 nm are formed on the basement of the broad unstructured band. Their intensities sequentially increase with the heat-treatment temperature in the range of 800–1000 °C while the intensity of the broad unstructured band has a non-monotonic behavior. The maximum intensity of the latter band is observed in GC prepared by the heat-treatment at the second stage of 850 and 900 °C, then it slightly decreases and remains unchanged for GCs prepared at 950-1050 °C (Fig. 16). The intensities of the peaks with maxima at 667, 676, 688, 698, 709, and 717 nm slightly decrease in the spectrum of the GC prepared at 1050 °C.

The luminescence spectra of GCs prepared by heat-treatments at the second stage at 850 – 1050 °C can be considered as a superposition of spectral features of the Cr^{3+}:$MgAl_2O_4$ luminescence and the band underlying these features and the longer wavelength band attributed to high- and low-crystal field Cr^{3+} sites, respectively, in the amorphous residual phase [116,119].

6. Discussion

In this section, we aimed to describe our results by comparing the structure of ceramic and GC and the behavior of iron and impurity chromium ions in these two hosts, wherever it is possible. Previously, we used this approach in the study of Co:$ZnAl_2O_4$ transparent ceramic and GC [33]. Such a comparison clearly demonstrates the characteristic features of both materials. The XRD pattern of ceramics presents a single-phase spinel material. The XRD pattern of the Fe:$MgAl_2O_4$-based GC reveals a multiphase material exhibiting the strongly broadened diffraction peaks of spinel located at the same positions as for the ceramic, as well as broad peaks of low intensity due to precipitation of MAT ss nanosized crystals and a massive halo due to a high content of the residual highly siliceous glass, Fig. 16(a). A relatively low spinel crystalline fraction in GC becomes evident.

A comparison of Raman spectra of ceramic and GC helped us to find characteristic vibrations of spinel nanocrystals in the complex Raman spectrum of GC containing the features of the MAT ss and those of the residual glass. Previously, we were certain that spinel vibrations are too weak in intensity to be noticed in the spectra of GCs at the background of intense vibrations of MAT ss [60]. The most intense spinel band located at 409 cm^{-1} can be easily found because in this spectral range there are no modes of the MAT ss. Moreover, we managed to find the other bands typical for spinel nanocrystals only by comparison with the spectrum of ceramics. Now we can notice the peaks at 200, 251, 306, 409, 496, 668, 724 and 764 cm^{-1} in the spectrum of GC and attribute them to vibrations connected with spinel crystals, Fig. 16(b).

The comparison of absorption spectra of ceramic and GC, Fig. 16(c), clearly indicates the presence of iron ions in ceramics only in one oxidation state, Fe^{2+}, and predominantly in the T_d sites as opposed to multiple valence states and different coordinations in GCs. This difference is the result of different phase compositions of the materials. The ceramic is a single-phase spinel while the GCs are multiphase materials containing spinel nanocrystals. Indeed, the glass under study demonstrates the three-phase immiscibility, i.e., formation of the magnesium aluminotitanate amorphous phase and an amorphous phase enriched in magnesia and alumina. These phases are located in the residual silica-rich glass. In fact, Fe ions are distributed between these three phases according to a partition coefficient. During further crystallization within amorphous regions enriched in magnesia and alumina and magnesium aluminotitanate amorphous regions, iron ions become a component of the spinel and MAT ss crystals, as well as remain in the residual glass. In the GCs, iron ions are located in spinel nanocrystals as $^{IV}Fe^{2+}$ and $^{VI}Fe^{2+}$, $^{IV}Fe^{3+}$ and $^{VI}Fe^{3+}$ species, in the MAT ss probably as $^{IV}Fe^{2+}$ species and predominantly in the form of Fe^{3+} species in the residual glass enriched in silica. The spinels in the ceramic and GCs are very different due to their different structures (i.e., different degree of inversion determined by composition and fabrication conditions), compositions (in GCs as opposed to ceramics, there are solid solutions of spinel enriched in alumina and containing titanium ions) and sizes (nm-sized in GCs vs. μm-sized in ceramic).

The luminescence spectra of both materials are very similar, Fig. 16(d). They are formed by luminescence of Cr^{3+} ions substituting for Al^{3+} ions in spinel crystals. The only difference in the spectra is the presence of a broad unstructured band with two maxima at about 720 and 750 nm observed in the spectrum of GCs. It is connected to a multiphase nature of GCs: this broad unstructured luminescence band is typical for Cr^{3+} ions in glass and reflects the presence of the residual glass in GCs. The maximum at about 720 nm on this broad band can be connected with the luminescence of Fe^{3+} ions in O_h symmetry in the Al^{3+} position in spinel nanocrystals in GCs [49-51].

We are aware that spinel ceramic often contains an admixture of secondary phases, i.e., kyanite ($Al_2O_3 \cdot SiO_2$) [51], $(MgO)_{0.91}(FeO)_{0.09}$ or periclase (MgO) [49,50]. These phases are manifested by luminescence of Fe^{3+} ions. The absence of Fe^{3+} ion luminescence in spinel ceramics proves that it is a single-phase material that does not contain Fe^{3+} ions.

Let us also comment on the synthesis method of our ceramics. In contrast to [47] where the Fe^{2+}:$MgAl_2O_4$ powders were obtained by laser ablation followed by free vacuum sintering, in our work the powders were synthesized by sol-gel method, and their consolidation was carried out by hot pressing in the presence of LiF sintering additive. This approach made it possible to obtain higher optical quality ceramics, which is especially noticeable in the visible and near-IR wavelength ranges. In addition, the main part of the iron remained in the +2 oxidation state in T_d sites. Thus, at close initial concentration of iron in spinel powders as compared to [47], the absorption of Fe^{2+} ions in our ceramics is several times greater, see Fig. 6(a).

7. Conclusions

We fabricated and studied the structure, phase transformations, optical and spectroscopic properties of the $Fe:MgAl_2O_4$ (spinel) transparent ceramic and $Fe:MgAl_2O_4$-based transparent nanophase glass-ceramics. The main difference of two materials is their phase composition which determines the valence state and coordination of the iron ions leading to different spectroscopic properties. The 0.1 mol% $Fe:MgAl_2O_4$ ceramic obtained by hot-pressing at 1600 °C / 50 MPa of powders obtained by the sol-gel method and using LiF as a sintering aid is a single-phase material being isostructural to undoped spinel (sp. gr. $Fd\bar{3}m$, the lattice constant a = 8.083±0.003 Å). Its microstructure is determined by relatively large grains (mean size: 50 μm) with clean grain boundaries and the lack of any secondary phases at their boundaries. The iron ions are replacing the Mg^{2+} ones in tetrahedral (T_d) sites. The optical absorption and visible luminescence studies indicated that the content of the $^{VI}Fe^{2+}$ and Fe^{3+} species, if present, is very low. The absorption of the $Fe:MgAl_2O_4$ ceramic is determined by a broad and intense band related to the $^5E \rightarrow {}^5T_2$ (^5D) transition of Fe^{2+} ions in T_d sites and corresponding to a ground-state absorption cross section of 0.28×10^{-18} cm^2 at the peak wavelength of 1.90 μm. This absorption band is similar in shape to that observed in Fe^{2+}-doped zinc chalcogenides (ZnS, ZnSe) while is blue-shifted.

This is for the first time that transparent $Fe:MgAl_2O_4$-based glass-ceramics were obtained. They were fabricated by secondary two-stage heat-treatment of the initial magnesium aluminosilicate glass nucleated by 10 mol% TiO_2 and doped with 0.1 mol% FeO. A complex picture of phase transformations in the initial glass and further in the GCs was determined. For the second stage of the heat-treatment at 800 – 1000 °C for 6 h (the first, nucleation, stage, was at 750 °C for 6 h), nanosized spinel crystals (mean size: 3.7 – 7.4 nm, lattice constant: a = 8.002 – 8.079 Å, both increasing with the heat-tretment temperature) precipitated. The transparent GCs were multi-phase materials containing, together with the spinel nanophase magnesium aluminotitanate solid solution (MAT ss) nanocrystals (mean size: 6.4-20.6 nm), as well as enriched in silica residual glass phase. The iron ions in these GCs were present as $^{IV}Fe^{2+}$, $^{VI}Fe^{2+}$ and Fe^{3+} species in the spinel structure, as well as Fe^{2+} and Fe^{3+} species in magnesium aluminotitanate solid solutions and in the residual glass. The presence of Ti^{3+} and Ti^{4+} ions (from the crystallization catalyst) determined the absorption of GCs in the UV-visible spectral range. Absorption is partly caused by interplay of iron and titanium ions in different valence states, coordination sites, and locations while the Cr^{3+} ions in spinel and in the residual glass (an uncontrolled impurity) determined the spectrum of visible luminescence.

In the present paper, we focused on revealing the nature of the optically active iron centers in spinel transparent ceramic and GCs. This is of key importance for potential applications of such materials, e.g., as laser gain media and saturable absorbers of mid-infrared lasers emitting at the wavelength of 2-3 μm. For applications, particularly the Fe^{2+} ions in T_d

sites are preferable. Besides, one cannot neglect the difference in the thermo-mechanical properties of the host materials and especially their resistance to the laser-induced damage which is much higher for GCs. Further work on Fe:MgAl$_2$O4 based transparent materials should focus on revealing their mid-infrared emission properties (the spectrum and the lifetime), as well as the saturable absorption properties. The latter may serve as an independent tool to confirm the ground-state absorption cross sections for $^{IV}Fe^{2+}$ species in spinel.

Acknowledgements

This work was partly supported by the RFBR (Grant 19-03-00855). The work at ICh-HPS was performed within the state assignment No. 0095-2019-005.

References

1. S. Mirov, V. Fedorov, I. Moskalev, D. Martyshkin, C. Kim, Progress in Cr^{2+} and Fe^{2+} doped mid-IR laser materials, Laser Photon. Rev. 4 (2010) 21-41.
2. A.A. Voronov, V.I. Kozlovskii, Y.V. Korostelin, A.I. Landman, Y.P. Podmar'kov, Y.K. Skasyrskii, M.P. Frolov, A continuous-wave Fe^{2+}:ZnSe laser, Quantum Electron. 38 (2008) 1113.
3. U. Demirbas, A. Sennaroglu, M. Somer, Synthesis and characterization of diffusion-doped Cr^{2+}:ZnSe and Fe^{2+}:ZnSe, Opt. Mater. 28 (2006) 231-240.
4. A.A. Voronov, V.I. Kozlovskii, Y.V. Korostelin, A.I. Landman, Y.P. Podmar'kov, V.G.~~E.~~ Polushkin, M.P. Frolov, Passive Fe^{2+}:ZnSe single-crystal Q switch for 3-μm lasers, Quantum Electron. 36 (2006) 1-2.
5. K.N. Firsov, E.M. Gavrishchuk, V.B. Ikonnikov, S.Y. Kazantsev, I.G. Kononov, S.A. Rodin, D.V. Savin, N.A. Timofeeva, High-energy room-temperature Fe^{2+}:ZnS laser, Laser Phys. Lett. 13 (2015) 015001-1-7.
6. M.E. Doroshenko, H. Jelínková, P. Koranda, J. Šulc, T.T. Basiev, V.V. Osiko, V.K. Komar, A.S. Gerasimenko, V.M. Puzikov, V.V. Badikov, D.V. Badikov, Tunable mid-infrared laser properties of Cr^{2+}:ZnMgSe and Fe^{2+}:ZnSe crystals, Laser Phys. Lett. 7 (2009) 38-45.
7. B. Denker, V. Dorofeev, B. Galagan, Y. Korostelin, V. Kozlovsky, S. Motorin, S. Sverchkov, Short pulse formation in a 2.3 μm Tm-doped tellurite glass laser by an Fe^{2+}:ZnS saturable absorber, Laser Phys. Lett. 15 (2018) 105801-1-4.
8. H. Cankaya, U. Demirbas, A.K. Erdamar, A. Sennaroglu, Absorption saturation analysis of Cr^{2+}:ZnSe and Fe^{2+}:ZnSe, J. Opt. Soc. Am. B 25 (2008) 794-800.
9. I. Ganesh, A review on magnesium aluminate ($MgAl_2O_4$) spinel: synthesis, processing and applications, Intern. Mater. Rev. 58 (2013) 63-112.
10. B. Schulz, Thermophysical properties of sapphire, AlN and $MgAl_2O_4$ down to 70 K, J. Nucl. Mater. 212 (1994) 1065-1068.
11. I. Kaprálik, Thermal expansion of spinels $MgCr_2O_4$, $MgAl_2O_4$ and $MgFe_2O_4$, Chem. Zvesti 23 (1969) 665 – 670.
12. N.V. Kuleshov, V.P. Mikhailov, V.G. Scherbitsky, P.V. Prokoshin, K.V. Yumashev, Absorption and luminescence of tetrahedral Co^{2+} ion in $MgAl_2O_4$, J. Lumin. 55 (1993) 265-269.
13. N.V. Kuleshov, V.G. Shcherbitsky, V.P. Mikhailov, S. Kück, J. Koetke, K. Petermann, G. Huber, Spectroscopy and excited-state absorption of Ni^{2+}-doped $MgAl_2O_4$, J. Lumin. 71 (1997) 265-268.

14. W. Stręk, P. Dereń, B. Jeżowska-Trzebiatowska, Optical properties of Cr^{3+} in $MgAl_2O_4$ spinel, Physica B Condens. Matter, 152 (1988) 379-384.

15. G. Karlsson, V. Pasiskevicius, F. Laurell, J.A. Tellefsen, B. Denker, B.I. Galagan, V.V. Osiko, S. Sverchkov, Diode-pumped Er–Yb:glass laser passively Q switched by use of Co^{2+}:$MgAl_2O_4$ as a saturable absorber, Appl. Opt. 39 (2000) 6188-6192.

16. A. Goldstein, P. Loiko, Z. Burshtein, N. Skoptsov, I. Glazunov, E. Galun, N. Kuleshov, K. Yumashev, Development of saturable absorbers for laser passive Q-switching near 1.5 μm based on transparent ceramic Co^{2+}:$MgAl_2O_4$, J. Am. Ceram. Soc. 99 (2016) 1324–1331.

17. G.B. Andreozzi, S. Lucchesi, Intersite distribution of Fe^{2+} and Mg in the spinel (sensu stricto)–hercynite series by single-crystal X-ray diffraction, Amer. Miner. 87 (2002) 1113-1120.

18. E.S. Gaffney, Spectra of Tetrahedral Fe^{2+} in $MgAl_2O_4$, Phys. Rev. B 8 (1973) 3484.

19. G.A. Slack, $FeAl_2O_4$-$MgAl_2O_4$: growth and some thermal, optical, and magnetic properties of mixed single crystals, Phys. Rev. 134 (1964) A1268-A1279.

20. G.A. Slack, F.S. Ham, R.M. Chrenko, Optical absorption of tetrahedral Fe^{2+} ($3d^6$) in cubic ZnS, CdTe, and $MgAl_2O_4$, Phys. Rev. 152 (1966) 376-402.

21. M.N. Taran, M. Koch-Müller, K. Langer, Electronic absorption spectroscopy of natural (Fe^{2+}, Fe^{3+})-bearing spinels of spinel ss-hercynite and gahnite-hercynite solid solutions at different temperatures and high-pressures, Phys. Chem. Mineral. 32 (2005) 175-188.

22. C.R. Jackson, L.C. Cheek, K.B. Williams, K.D. Hanna, C.M. Pieters, S.W. Parman, R.F. Cooper, M.D. Dyar, M. Nelms, M.R. Salvatore, Visible-infrared spectral properties of iron-bearing aluminate spinel under lunar-like redox conditions, Amer. Miner. 99 (2014) 1821-1833.

23. U. Hålenius, H. Skogby, G.B. Andreozzi, Influence of cation distribution on the optical absorption spectra of Fe^{3+}-bearing spinel ss–hercynite crystals: evidence for electron transitions in $^{VI}Fe^{2+}$–$^{VI}Fe^{3+}$ clusters, Phys. Chem. Mineral. 29 (2002) 319-330.

24. B. Cockayne, M. Chesswas, The vertical pulling of $MgAl_2O_4$ single crystals, J. Mater. Sci. 2 (1967) 498-500.

25. Y.V. Volk, A.M. Malyarevich, K.V. Yumashev, V.N. Matrosov, T.A. Matrosova, M.I. Kupchenko, Anisotropy of nonlinear absorption in Co^{2+}:$MgAl_2O_4$ crystal, Appl. Phys. B 88 (2007) 443-447.

26. R.K. Sackuvich, J.M. Peppers, N.S. Myoung, V.V. Badikov, V.V. Fedorov, S.B. Mirov, Spectroscopic characterization of Ti^{3+}:$AgGaS_2$ and Fe^{2+}:$MgAl_2O_4$ crystals for mid-IR laser applications, Solid State Lasers XXI: Technology and Devices, edited by W. Andrew Clarkson, Ramesh K. Shori, Proc. SPIE 8235 (2012), 823520-1-6.

27. R. Reisfeld, A. Kisilev, E. Greenberg, A. Buch, M. Ish-Shalom, Spectroscopy of Cr(III) in transparent glass ceramics containing spinel and gahnite, Chem. Phys. Lett. 104 (1984) 153-156.

28. A.M. Malyarevich, I.A. Denisov, K.V. Yumashev, O.S. Dymshits, A.A. Zhilin, Optical absorption and luminescence study of cobalt-doped magnesium aluminosilicate glass ceramics, J. Opt. Soc. Am. B 19 (2002) 1815-1821.

29. P.A. Loiko, O.S. Dymshits, N.A. Skoptsov, A.M. Malyarevich, A.A. Zhilin, I.P. Alekseeva, M.Y. Tsenter, K.V. Bogdanov, X. Mateos, K.V. Yumashev, Crystallization and nonlinear optical properties of transparent glass-ceramics with Co:$Mg(Al,Ga)_2O_4$ nanocrystals for saturable absorbers of lasers at 1.6–1.7 μm, J. Phys. Chem. Sol. 103 (2017) 132-141.

30. A. Goldstein, A. Krell, Transparent ceramics at 50: progress made and further prospects, J. Am. Ceram. Soc. 99 (2016) 3173–3197.

31. A.V. Belyaev, I.I. Evdokimov, V.V. Drobotenko, A.A. Sorokin, A new approach to producing transparent $ZnAl_2O_4$ ceramics, J. Eur. Ceram. Soc. 37 (2017) 2747–2751.
32. L. Wei, Y. Pan, C. Li, H. Kou, J. Li, Fabrication and spectral properties of hot-pressed Co:$MgAl_2O_4$ transparent ceramics for saturable absorber, J. Alloys Compd. 724 (2017) 45–50.
33. P. Loiko, A. Belyaev, O. Dymshits, I. Evdokimov, V. Vitkin, K. Volkova, M. Tsenter, A. Volokitina, M. Baranov, E. Vilejshikova, A. Baranov, A Zhilin, Synthesis, characterization and absorption saturation of Co:$ZnAl_2O_4$ (gahnite) transparent ceramic and glass-ceramics: A comparative study, J. Alloy Compd. 725 (2017) 998–1005.
34. S.S. Balabanov, R.P. Yavetskiy, A.V. Belyaev, E.M. Gavrishchuk, V.V. Drobotenko, I.I. Evdokimov, A.V. Novikova, O.V. Palashov, D.A. Permin, V.G. Pimenov, Fabrication of transparent $MgAl_2O_4$ ceramics by hot-pressing of sol-gel-derived nanopowders, Ceram. Intern. 41 (2015) 13366-13371.
35. S. Su, Q. Liu, Z. Hu, X. Chen, H. Pan, X. Liu, L. Wu, J. Li, A simple way to prepare Co:$MgAl_2O_4$ transparent ceramics for saturable absorber, J. Alloy~~s~~ Compd. 797 (2019) 1288-1294.
36. S.S. Balabanov, A.V. Belyaev, A.V. Novikova, D.A. Permin, E.Ye. Rostokina, R.P. Yavetskiy, Densification peculiarities of transparent $MgAl_2O_4$ ceramics - Effect of LiF sintering additive, Inorg. Mater. 54 (2018) 1045-1050.
37. D. Han, J. Zhang, P. Liu, G. Li, L. An, S. Wang, Preparation of high-quality transparent Al-rich spinel ceramics by reactive sintering, Ceram. Intern. 44 (2018) 3189-3194.
38. M.K. Alekseev, G.I. Kulikova, M.Yu. Rusin, N.N. Savanina, S.S. Balabanov, A.V. Belyaev, E.M. Gavrishchuk, A.V. Ivanov, R.N. Rizakhanov, Transparent ceramics prepared from ultrapure magnesium aluminate spinel nanopowders by spark plasma sintering, Inorg. Mater. 52 (2016) 324–330.
39. Yu.V. Bykov, S.V. Egorov, A.G. Eremeev, V.V. Kholoptsev, I.V. Plotnikov, K.I. Rybakov, A.A. Sorokin, S.S. Balabanov, A.V. Belyaev, Ultra-rapid microwave sintering of pure and Y_2O_3-doped $MgAl_2O_4$, J. Am. Ceram. Soc.102 (2019) 559-568.
40. M. Rubat Du Merac, H.J. Kleebe, M.M., Müller, I.E. Reimanis, Fifty years of research and development coming to fruition; Unraveling the complex interactions during processing of transparent magnesium aluminate ($MgAl_2O_4$) spinel, J. Am. Ceram. Soc. 96 (2013) 3341–3365.
41. S.S. Balabanov, V.E. Vaganov, E.M. Gavrishchuk, V.V. Drobotenko, D.A. Permin, A.V. Fedin, Effect of magnesium aluminum isopropoxide hydrolysis conditions on the properties of magnesium aluminate spinel powders, Inorg. Mater. 50 (2014) 830–836.
42. J. Sanghera, S. Bayya, G. Villalobos, W. Kim, J. Frantz, B. Shaw, B. Sadowski, R. Miklos, C.C. Baker, M. Hunt, I.D. Aggarwal, F. Kung, D. Reicher, S. Peplinski, A. Ogloza, P.F. Langston, C. Lamar, P. Varmette, M. Dubinskiy, L. DeSandre, Transparent ceramics for high-energy laser systems, Opt. Mater. 33 (2011) 511-518.
43. S.V. Egorov, A.A. Sorokin, I.E. Ilyakov, B.V. Shishkin, E.A. Serov, V.V. Parshin, K.I. Rybakov, S.S. Balabanov, A.V. Belyaev, Terahertz dielectric properties of polycrystalline $MgAl_2O_4$ spinel obtained by microwave sintering and hot pressing, J. Infrared Millim. Te. 40 (2019) 447-455.
44. G.H. Beall, L.R. Pinckney, Nanophase glass-ceramics, J. Amer. Ceram. Soc. 82 (1999) 5-16.

45. A.R. Molla, C.R. Kesavulu, R.P.S. Chakradhar, A. Tarafder, S.K. Mohanty, J.L. Rao, B. Karmakar, S.K. Biswas, Microstructure, mechanical, thermal, EPR, and optical properties of $MgAl_2O_4:Cr^{3+}$ spinel glass–ceramic nanocomposites, J. Alloy Compd. 583 (2014) 498-509.
46. V.V. Golubkov, O.S. Dymshits, A.A. Zhilin, T.I. Chuvaeva, A.V. Shashkin, The influence of nickel oxide additives on the phase separation and crystallization of glasses in the MgO-Al_2O_3-SiO_2-TiO_2 system, Glass Phys. Chem. 30 (2004) 300-310.
47. A. Dugué, O. Dymshits, L. Cormier, B. Cochain, G. Lelong, A. Zhilin, S. Belin, In situ evolution of Ni environment in magnesium aluminosilicate glasses and glass–ceramics–Influence of ZrO_2 and TiO_2 nucleating agents, J. Phys. Chem. Solids, 78 (2015) 137–146.
48. A. Dugué, O. Dymshits, L. Cormier, P. Loiko, I. Alekseeva, M. Tsenter, K. Bogdanov, G. Lelong, A. Zhilin, Structural transformations and spectroscopic properties of Ni-doped magnesium aluminosilicate glass-ceramics nucleated by a mixture of TiO_2 and ZrO_2 for broadband near-IR light emission, J. Alloys Compd. 780 (2019) 137-146.
49. V.V. Osipov, V.A. Shitov, R.N. Maksimov, K.E. Lukyashin, V.I. Solomonov, A.V. Ishchenko, Fabrication and characterization of IR-transparent Fe^{2+} doped $MgAl_2O_4$ ceramics, J. Amer. Ceram. Soc. 102 (2019) 4757-4764.
50. V.V. Osipov, V.A. Shitov, K.E. Luk'yashin, V.V. Platonov, V.I. Solomonov, A.S. Korsakov, A.I. Medvedev, Quantum Electron. 49 (2019) 89-94.
51. A.S. Bubnova, V.I. Solomonov, Luminescence analysis of ceramic magnesium aluminum spinel $Fe^{2+}:MgAl_2O_4$ synthesized from nanosized powders via syntering in air and vacuum, AIP Conf. Proc. 2174 (2019) 020087-1-5.
52. K. Eremeev, O. Dymshits, I. Alekseeva, A. Khubetsov, S. Zapalova, M. Tsenter, L. Basyrova, P. Loiko, A. Zhilin, V. Popkov, Spectral properties of novel transparent glass-ceramics based on $Fe^{2+}:ZnAl_2O_4$ nanocrystals, J. Phys. Conf. Ser. 1697 (2020) 012125.
53. K. Eremeev, O. Dymshits, I. Alekseeva, A. Khubetsov, M. Tsenter, A. Zhilin, L. Basyrova, P. Loiko, V. Popkov, The influence of the Fe^{2+} doping concentration on structure and spectroscopic properties of transparent glass-ceramics based on $Fe^{2+}:ZnAl_2O_4$ nanocrystals, J. Phys. Conf. Ser. 1965 (2020) 012011.
54. L. Lin, R. Miao, W. Xie, J. Chen, Y. Zhao, Z. Wu, J. Qiu, H. Yu, S. Zhou, In situ and tunable structuring of semiconductor-in-glass transparent composite, iScience 24 (2021) 101984.
55. S. Wang, Effects of Fe on crystallization and properties of a new high infrared radiance glass-ceramics. Environ. Sci. Technol. 44 (2010) 4816-4820.
56. S. M. Wang, F. H. Kuang, Q. Z. Yan, C. C. Ge, L. H. Qi, Crystallization and infrared radiation properties of iron ion doped cordierite glass-ceramics. J. Alloys Compd. 509 (2011) 2819-2823.
57. T. Liu, Q. Huang, H. Liang, P. Liu, Z. Luo, L. Zhu, A. Lu, Effect of Fe_2O_3 doping on structure, physical-mechanical properties and luminescence performance of magnesium-aluminum-silicon based glass-ceramics. Ceram. Int. 46, (2020) 28851-28859.
58. V. Bukina, O. Dymshits, I. Alekseeva, M. Tsenter, S. Zapalova, A. Khubetsov, A. Zhilin, L. Basyrova, A. Volokitina, P. Loiko, Optical glass-ceramics based on nanosized crystals of magnesium aluminate spinel doped with iron ions, J. Phys. Conf. Ser. 1697 (2020) 012156.
59. V. Bukina, L. Basyrova, O. Dymshits, I. Alekseeva, M. Tsenter, S. Zapalova, A. Khubetsov, A. Volokitina, A. Zhilin, P. Loiko, Novel transparent glass-ceramics based on $Fe^{2+}:MgAl_2O_4$ spi-

nel nanocrystals, *in 2020 International Conference Laser Optics (ICLO)*, St. Petersburg, Russia, 2-6 November, 2020 (IEEE), P. ThR1-p02, doi: 10.1109/ICLO48556.2020.9285568.

60. O.S. Dymshits, A.A. Zhilin, V.I. Petrov, M. Tsenter, Ya, T.I. Chuvaeva, A.V. Shashkin, V.V. Golubkov, U. Kang, K.H. Lee, Raman spectroscopic study of phase transformations in titanium-containing magnesium aluminosilicate glasses, Glass Phys. Chem. 28 (2002) 66-78.

61. V.V. Golubkov, O.S. Dymshits, A.A. Zhilin, T.I. Chuvaeva, A.V. Shashkin, On the phase separation and crystallization of glasses in the MgO-Al_2O_3-SiO_2-TiO_2 system, Glass Phys. Chem. 29 (2003) 254-266.

62. H. Lipson, H. Steeple, in: McMillan (Ed.), Interpretation of X-ray Powder Patterns, Martins Press, London, N.Y., 1970, 344 p.

63. Y. Mordekovitz, L. Shelly, M. Halabi, S. Kalabukhov, S. Hayun, The effect of lithium doping on the sintering and grain growth of SPS-processed, non-stoichiometric magnesium aluminate spinel, Materials, 9 (2016) 481-1-12.

64. H. Sawada, An electron density residual study of magnesium aluminum oxide spinel, Mater. Res. Bull. 30 (1995) 341-345.

65. D. Simeone, C. Dodane, D. Gosset, P. Daniel, M. Beauvy, Order–disorder phase transition induced by swift ions in $MgAl_2O_4$ and $ZnAl_2O_4$ spinels. J. Nucl. Mat. 300 (2002) 151–160.

66. K.E. Sickafus, Comment on ‘order–disorder phase transition induced by swift ions in $MgAl_2O_4$ and $ZnAl_2O_4$ spinels’ by Simeone et al., J. Nucl. Mat. 312 (2003) 111–123.

67. P. Barpanda, S.K. Behera, P.K. Gupta, S.K. Pratihar, S. Bhattacharya, Chemically induced order disorder transition in magnesium aluminium spinel, J. Eur. Ceram. Soc. 26 (2006) 2603–2609.

68. M. Ardit, G. Cruciani, M. Dondi, Structural relaxation in tetrahedrally coordinated Co^{2+} along the gahnite-Co-aluminate spinel solid solution, Amer. Mineralog. 97 (2012) 1394-1401.

69. R.J. Harrison, S.A. Redfern, H.S.C. O’Neill, The temperature dependence of the cation distribution in synthetic hercynite ($FeAl_2O_4$) from in-situ neutron structure refinements, Amer. Miner. 83 (1998) 1092-1099.

70. R.D. Shannon, Revised effective ionic radii and systematic studies of interatomic distances in halides and chalcogenides, Acta Crystallogr. 32 (1976) 751-767.

71. M. P. O'Horo, A. L. Frisillo, W. B. White, Lattice vibrations of $MgAI_2O_4$ spinel, J. Phys. Chem. Solids, 34 (1973) 23-28.

72. H. Cynn, S.K. Sharma, T.F. Cooney, M. Nicol, High-temperature Raman investigation of order-disorder behavior in the $MgAl_2O_4$ spinel, Phys. Rev. B 45 (1992) 500-502.

73. G.A. de Wijs, C.M. Fang, G. Kresse, G. de With, First-principles calculation of the phonon spectrum of $MgAl_2O_4$ spinel, Phys. Rev. B 65 (2002) 094305-1-5.

74. S. Slotznick, S.-H. Shim, In situ Raman spectroscopy measurements of $MgAl_2O_4$ spinel up to 1400 °C, Amer. Miner. 93 (2008) 470–476.

75. V. D'Ippolito, G.B. Andreozzi, P.P. Lottici, D. Bersani, Raman study of $MgAl_2O_4$–$FeAl_2O_4$ and $MgAl_2O_4$–$MgFe_2O_4$ spinel solid solutions, Period. di Mineral., ECMS 2015 (2015) 61-62.

76. S. Jiang, T. Lu, Y. Long, J. Chen, Ab initio many-body study of the electronic and optical properties of $MgAl_2O_4$ spinel, J. Appl. Phys. 111 (2012) 043516.

77. G.R. Rossman, M.N. Taran, Spectroscopic standards for four- and fivefold-coordinated Fe^{2+} in oxygen-based minerals, Amer. Miner. 86 (2001) 896–903.

78. M.N. Taran, K. Langer, Electronic absorption spectra of Fe^{2+} ions in oxygen-based rock-forming minerals at temperatures between 297 and 600 K, Phys. Chem. Miner. 28 (2001) 199–210.
79. H. Skogby, U. Hålenius, An FTIR study of tetrahedrally coordinated ferrous iron in the spinel-hercynite solid solution, Amer. Miner. 88 (2003) 489–492.
80. V. D'Ippolito, G.B. Andreozzi, U. Hålenius, H. Skogby, K. Hametner, D.F Günther, Color mechanisms in spinel: cobalt and iron interplay for the blue color, Phys. Chem. Miner. 42 (2015) 431–439.
81. B.L. Dickson, G. Smith, Low-temperature optical absorption and Mössbauer spectra of staurolite and spinel, Canad. Mineral. 14 (1976) 206-215.
82. E. Bruschini, S. Speziale, F. Bosi, G.B. Andreozzi, Fe–Mg substitution in aluminate spinels: effects on elastic properties investigated by Brillouin scattering, Phys. Chem. Miner. 45 (2018) 759–772.
83. P.B. Devaraja, D.N. Avadhani, H. Nagabhushana, S.C. Prashantha, S.C. Sharma, B.M. Nagabhushana, H.P. Nagaswarupa, B.D. Prasad, Luminescence properties of $MgO:Fe^{3+}$ nanopowders for WLEDs under NUV excitation prepared via propellant combustion route, J. Radiat. Res. Appl. Sci. 8 (2015) 362-373.
84. T.R. N. Kutty, M. Nayak, Cationic distribution and its influence on the luminescent properties of Fe^{3+}-doped $LiAl_5O_8$ prepared by wet chemical methods, J. Alloys Compd. 269 (1998) 75-87.
85. L.P. Sosman, A. Dias Tavares Jr, P.S. Silva, T. Abritta, Optical spectroscopy of $MgGa_2O_4$: Fe^{3+}, Phys. Status Solidi A 176 (1999)1085-1088.
86. D.L. Wood, G.F. Imbush, R.M. Macfarlane, P. Kisliuk, D.M. Larkin, Optical Spectrum of Cr^{3+} ions in spinels, J. Chem. Phys. 48 (1968) 5255-5263.
87. M.G. Brik, J. Papan, D.J. Jovanović, M.D. Dramićanin, Luminescence of Cr^{3+} ions in $ZnAl_2O_4$ and $MgAl_2O_4$ spinels: correlation between experimental spectroscopic studies and crystal field calculations, J. Lumin. 177 (2016) 145–151.
88. D.M. Sherman, Reassignment of the iron(III) absorption bands in the spectra of Mars, Lunar Planetary Sci. 15 (1984) 764-765.
89. J.B. Higgins, P.H. Ribbe, R.K. Herd, Sapphirine I. Crystal chemical contributions, Contrib. Mineral. Petrol. 68 (1979) 349-356.
90. J. W. Anthony, R. A. Bideaux, K. W. Bladh, M. C. Nichols, Eds., Handbook of Mineralogy, Mineralogical Society of America, Chantilly, VA 20151-1110, USA, http://www.handbookofmineralogy.com/pdfs/sapphirine.pdf
91. J. W. Anthony, R. A. Bideaux, K. W. Bladh, M. C. Nichols, Eds., Handbook of Mineralogy, Mineralogical Society of America, Chantilly, VA 20151-1110, USA, http://www.handbookofmineralogy.com/pdfs/armalcolite.pdf
92. T. Kawasaki, T. Adachi, N. Nakano, Y. Osanai, Possible armalcolite pseudomorph-bearing garnet–sillimanite gneiss from Skallevikshalsen, Lützow-Holm Complex, East Antarctica: Implications for ultrahigh-temperature metamorphism, Geological Society, London, Special Publications 383 (2013) 135-167.
93. http://rruff.info/sapphirine/display=default/
94. A. Tamura, K. Higeta, T. Ichinokawa, Lattice vibrations and specific heat of a small particle, J. Phys. C 15 (1982) 4975-4991.

95. V.I. Petrov, Ya.S. Bobovich, Raman scattering by acoustic phonons of TiO_2 submicrocrystals in glasses, Opt. Spectrosc. 67 (1989) 363-365.
96. B. Champagnon, B. Andrianasolo, E. Duval, Size determination of semiconductor nanocrystallites by low frequency inelastic scattering (LOFIS), Mater. Sci. Eng. B 9 (1991) 417–420.
97. T.I. Chuvaeva, O.S. Dymshits, V.I. Petrov, M.Ya. Tsenter, A.V. Shashkin, A.A. Zhilin, V.V. Golubkov, Low-frequency Raman scattering of magnesium aluminosilicate glasses and glass-ceramics, J. Non-Cryst. Solids 282 (2001) 306-316.
98. W.P. Mason, ed. Physical Acoustics, Applications to Quantum and Solid State Physics, 1968, Academic Press, New-York, London, 1968.
99. H.K. Mao, P.M. Bell, Crystal-field effects of trivalent titanium in fassaite from the Pueblo de Allende meteorite. Ann. Rep. Geophys. Lab., Carnegie Inst. Washington Yearb. 73 (1974) 488-492.
100. D.A. Nolet, R.G. Burns, S.L. Flamm, J.R. Besancon, Spectra of Fe-Ti silicate glasses: Implications to remote-sensing of planetary surfaces, in *Lunar and Planetary Science Conference Proceedings* (Vol. 10, pp. 1775-1786, 1979).
101. A.S. Marfunin, Physics of minerals and inorganic materials: an introduction, Springer-Verlag, Berlin, Heidelberg, New York, 1979, 340 pp.
102. B.M. Loeffler, R.G. Burns, J.A. Tossell, D.J. Vaughan, K.H. Johnson, Charge transfer in lunar materials: interpretation of ultraviolet-visible spectral properties of the moon, in *Lunar and Planetary Science Conference Proceedings* (vol. 5, pp. 3007-3016, 1974).
103. G.H. Faye, D.C. Harris, On the origin and pleochroism in andalusite from Brazil. Can. Mineral. 10 (1969) 47-56.
104. R.G. Burns, Intervalence transitions in mixed valence minerals of iron and titanium, Ann. Rev. Earth Planet. Sci. 9 (1981) 345-383.
105. V. Vercamer, G. Lelong, H. Hijiya, Y. Kondo, L. Galoisy, G. Calas, Diluted Fe^{3+} in silicate glasses: Structural effects of Fe-redox state and matrix composition. An optical absorption and X-band/Q-band EPR study, J. Non-Cryst. Solids 428 (2015) 138–145.
106. L. Galoisy, G. Calas, M.A Arrio, High-resolution XANES spectra of iron in minerals and glasses: structural information from the pre-edge region, Chem. Geol. 174 (2001) 307-319.
107. D. Virgo, B.O. Mysen, The structural state of iron in oxidized vs. reduced glasses at 1 atm: A ^{56}Fe Mössbauer study, Phys. Chem. Miner. 12 (1985) 65-76.
108. R. Ya. Khodakovskaya, Khimiya titansoderzhashchikh stekol i sitallov (Chemistry of Titanium-Containing Glasses and Glass Ceramics), Khimiya, Moscow, 1978 [in Russian].
109. B.O. Mysen, The structural behavior of ferric and ferrous iron in aluminosilicate glass near meta-aluminosilicate joins, Geochim. Cosmochim. Acta 70 (2006) 2337-2353.
110. V. D'Ippolito, G.B. Andreozzi, Linking crystal chemistry and physical properties of natural and synthetic spinels: an UV–VIS–NIR and Raman study, Doctoral dissertation, Sapienza Università di Roma, 2013, 237 pp.
111. J.S. Reed, H.F. Kay, Optical spectra of 3d transition metal ions in MgO $3.5Al_2O_3$ spinel, J. Am. Ceram. Soc. 52 (1969) 307-311.
112. D. Lenaz, H. Skogby, F. Nestola, F. Princivalle, OH incorporation in nearly pure $MgAl_2O_4$ natural and synthetic spinels, Geochim. Cosmochim. Acta 72 (2008) 475–479.
113. G.D. Bromiley, F. Nestola, S.A.T. Redfern, M. Zhang, Water incorporation in synthetic and natural $MgAl_2O_4$ spinel, Geochim. Cosmochim. Acta 74 (2010) 705–718.

114. A.S. Povarennykh, Crystal chemical classification of minerals, Springer, New York, 1972, 286 pp.
115. G. Steffen, F. Seifert, G. Amthauer, Ferric iron in sapphirine: a Mössbauer spectroscopic study, Amer. Miner. 69 (1984) 339-348.
116. G. Boulon, Luminescence in glassy and glass ceramic materials, Mater. Chem. Phys. 16 (187) 301-347.
117. Cz. Koepke, K. Wisniewski, M. Grinberg, Excited state spectroscopy of chromium ions in various valence states in glasses, J. Alloy Compd. 341 (2002) 19–27.
118. S.A. Brawer, W.B. White, Optical properties of trivalent chromium in silicate glasses: A study of energy levels in the crossing region, J. Chem. Phys. 67 (1977) 2043-2055.
119. V.C. Costa, F.S. Lameiras, M.V.B. Pinheiro, D.F. Sousa, L.A.O. Nunes, Y.R. Shen, K.L. Bray, Laser spectroscopy and electron paramagnetic resonance of Cr^{3+} doped silicate glasses, J. Non-Cryst. Solids 273 (2000) 209-214.

List of figure captions

Figure 1. Photograph of the laser-grade-polished undoped $MgAl_2O_4$ (*left*) and 0.1 mol% Fe:$MgAl_2O_4$ (*right*) transparent ceramic disks.

Figure 2. Photographs of the initial glass and transparent GCs obtained by various secondary heat-treatments, (temperature, °C / duration, h).

Figure 3. XRD patterns of an undoped $MgAl_2O_4$ ceramic and a 0.1 mol% Fe:$MgAl_2O_4$ ceramic; *numbers* denote the Miller's indices (*hkl*). The patterns are shifted for the convenience of observation. *Red peaks* – theoretical pattern for $MgAl_2O_4$ (ICSD card No. 82-2424).

Figure 4. (a) SEM image of a fracture surface of a 0.1 mol% Fe:$MgAl_2O_4$ ceramic; (b) a typical grain size distribution.

Figure 5. Unpolarized Raman spectra of an undoped $MgAl_2O_4$ ceramic and a 0.1% Fe:$MgAl_2O_4$ ceramic, λ_{exc} = 514 nm, *numbers* denote positions of the Raman peaks in cm^{-1}.

Figure 6. (a) In-line transmission spectra of laser-grade-polished undoped $MgAl_2O_4$ and 0.1 mol% Fe:$MgAl_2O_4$ ceramic disks (t = 1.0 mm), *green curve* indicates the theoretical Fresnel losses; (b) the absorption cross sections, σ_{abs}, for the $^5E \rightarrow {}^5T_2(^5D)$ transition of Fe^{2+} ions in T_d sites in $MgAl_2O_4$ ceramic, ZnSe and ZnS materials.

Figure 7. Luminescence spectrum of the 0.1 mol% Fe:$MgAl_2O_4$ ceramic. The excitation wavelength is 488 nm. *Numbers* denote the positions of the emission peaks in nm.

Figure 8. Variation of density with the heat-treatment temperature for the initial glass and glass-ceramics (for the samples heat-treated at 800 °C and above, the first stage is at 750 °C). The *line* serves as a guide for the eye. The error bars match the size of symbols.

Figure 9. DSC curves for the initial glass and the glass heat-treated at 750 °C for 6 h. T_g is the glass transition temperature, T_{on} is the crystallization onset temperature. The curves are shifted for the convenience of observation.

Figure 10. XRD patterns (a) of the initial glass heat-treated in the DSC furnace up to 915 and 1160 °C; (b) of the sample preheated at 750 °C for 6 h and heat-

treated in the DSC furnace up to 840, 970 and 1150 °C. The patterns are shifted for the convenience of observation.

Figure 11. XRD patterns of 0.1% Fe-doped the initial glass and transparent GCs. *Labels* 800 – 1050 °C indicate the heat-treatment temperature at the second stage (holding time: 6 h). The nucleation stage is at 750 °C for 6 h. o - spinel, x - magnesium aluminotitanate (MAT) solid solution (ss), v - sapphirine. The patterns are shifted for the convenience of observation.

Figure 12. TEM images of 0.1 wt.% Fe-doped (a) initial glass, (b) glass heat-treated at 750 °C for 6 h, and (c) glass heat-treated at 750 °C for 6 h and at 950 °C for 6 h. *Insets* in (b),(c) – size distributions of the nanocrystals. Note the different magnification.

Figure 13. Unpolarized Raman spectra of the initial glass and transparent glass-ceramics: (a) the overview of the frequency range of 100-1300 cm^{-1}, (b) a close look at the frequency range of 5-350 cm^{-1} with a notch filter. *Labels* 800 – 1050 °C indicate the heat-treatment temperature at the second stage. λ_{exc} = 514 nm, *numbers* denote the position of the Raman peaks in cm^{-1}. The curves are shifted for the convenience of observation.

Figure 14. Absorption spectra of the initial glass and transparent glass-ceramics in different spectral ranges: (a) overview spectrum, (b) a close look on the 0.3-2.4 µm range, (c) a close look on the OH^--group absorption at 2.6 – 3.2 µm. *Labels* 800 – 1050 °C indicate the heat-treatment temperature at the second stage. The first stage of the heat-treatment is always at 750 °C for 6 h. *Numbers* in (c) indicate the peak positions in nm.

Figure 15. Spectra of visible luminescence from the initial glass and transparent glass-ceramics. *Labels* 800 – 1050 °C indicate the heat-treatment temperature at the second stage. λ_{exc} = 488 nm.

Figure 16. Comparison of a 0.1 mol% Fe:$MgAl_2O_4$ ceramic and Fe:$MgAl_2O_4$ based glass-ceramics prepared by the heat-treatment with the second stage at 1000 °C for 6 h: (a) XRD patterns, (b) Raman spectra, λ_{exc} = 514 nm, *numbers* denote the Raman frequencies in cm^{-1}, (c) absorption spectra (for ceramics, the scattering losses are subtracted), and (d) spectra of visible luminescence, λ_{exc} = 488 nm, *numbers* denote the positions of the emission peaks in nm.

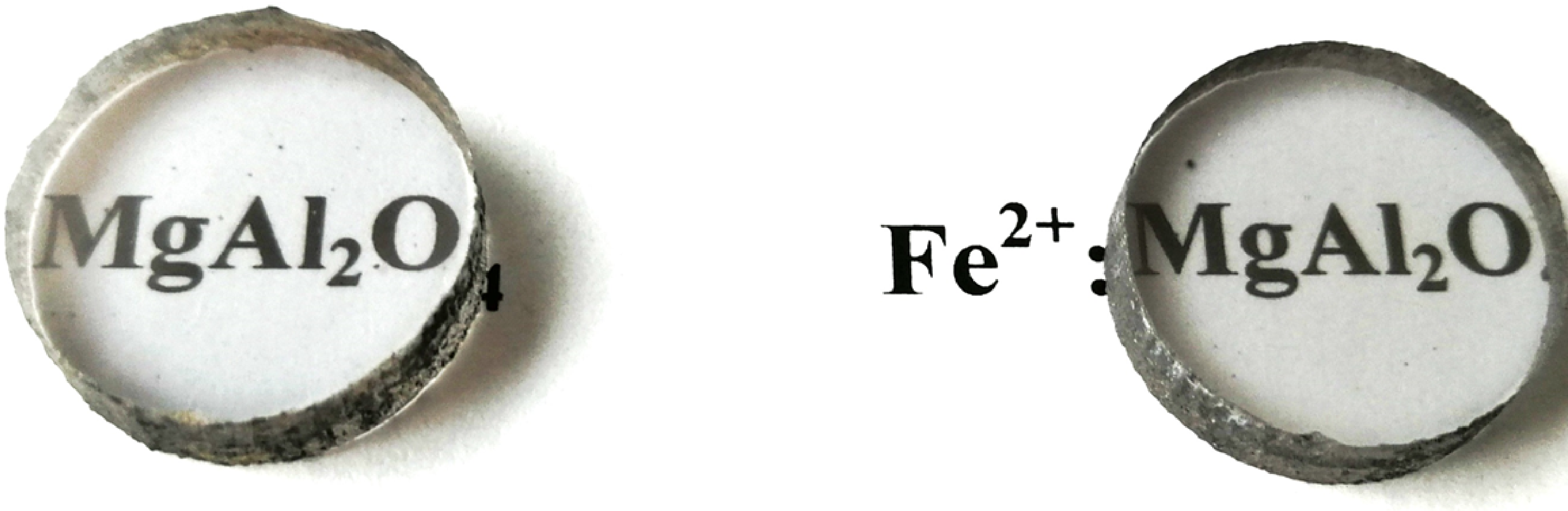
$MgAl_2O_4$
$Fe^{2+}:MgAl_2O$

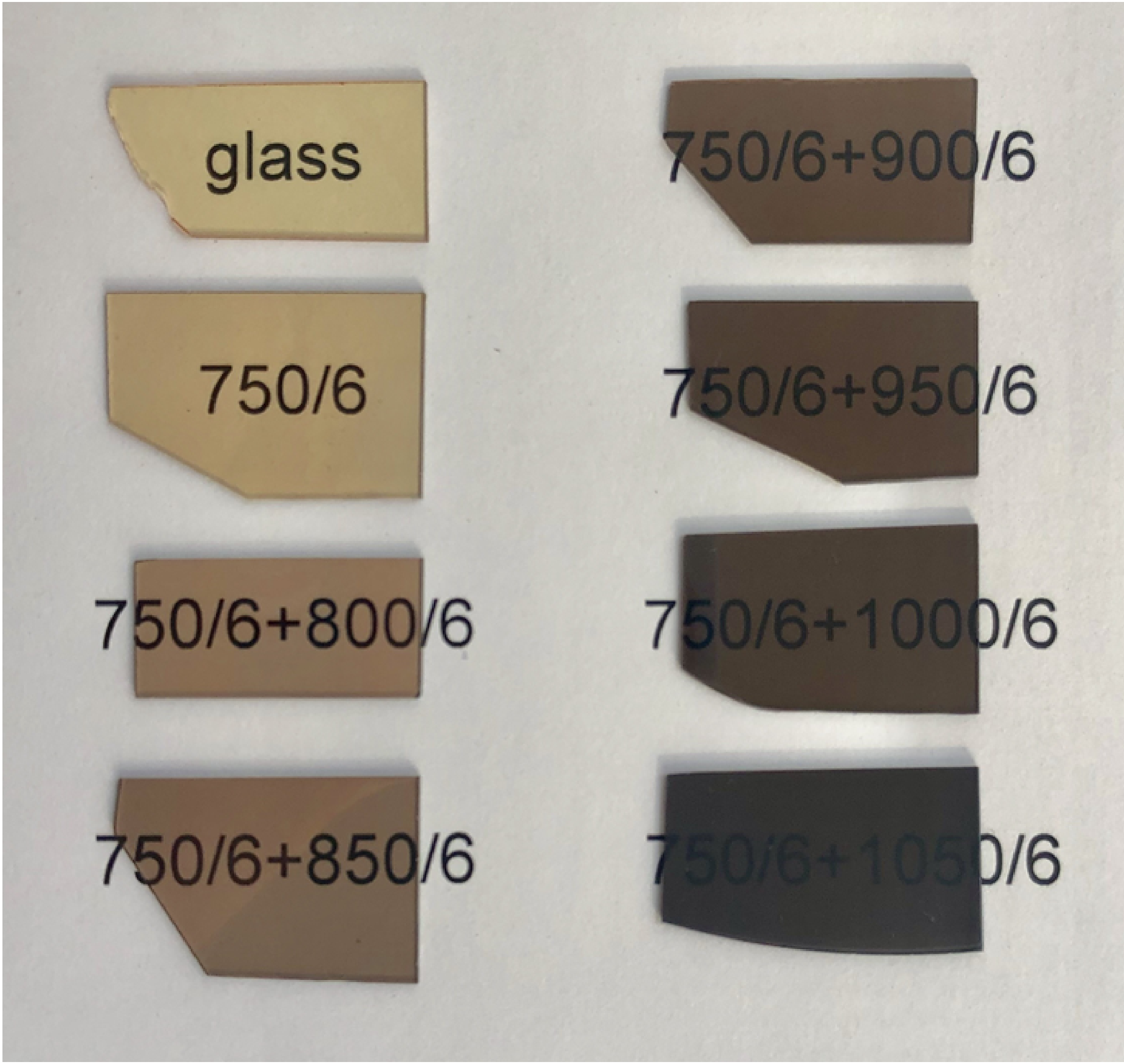
glass
750/6
750/6+800/6
750/6+850/6
750/6+900/6
750/6+950/6
750/6+1000/6
750/6+1050/6

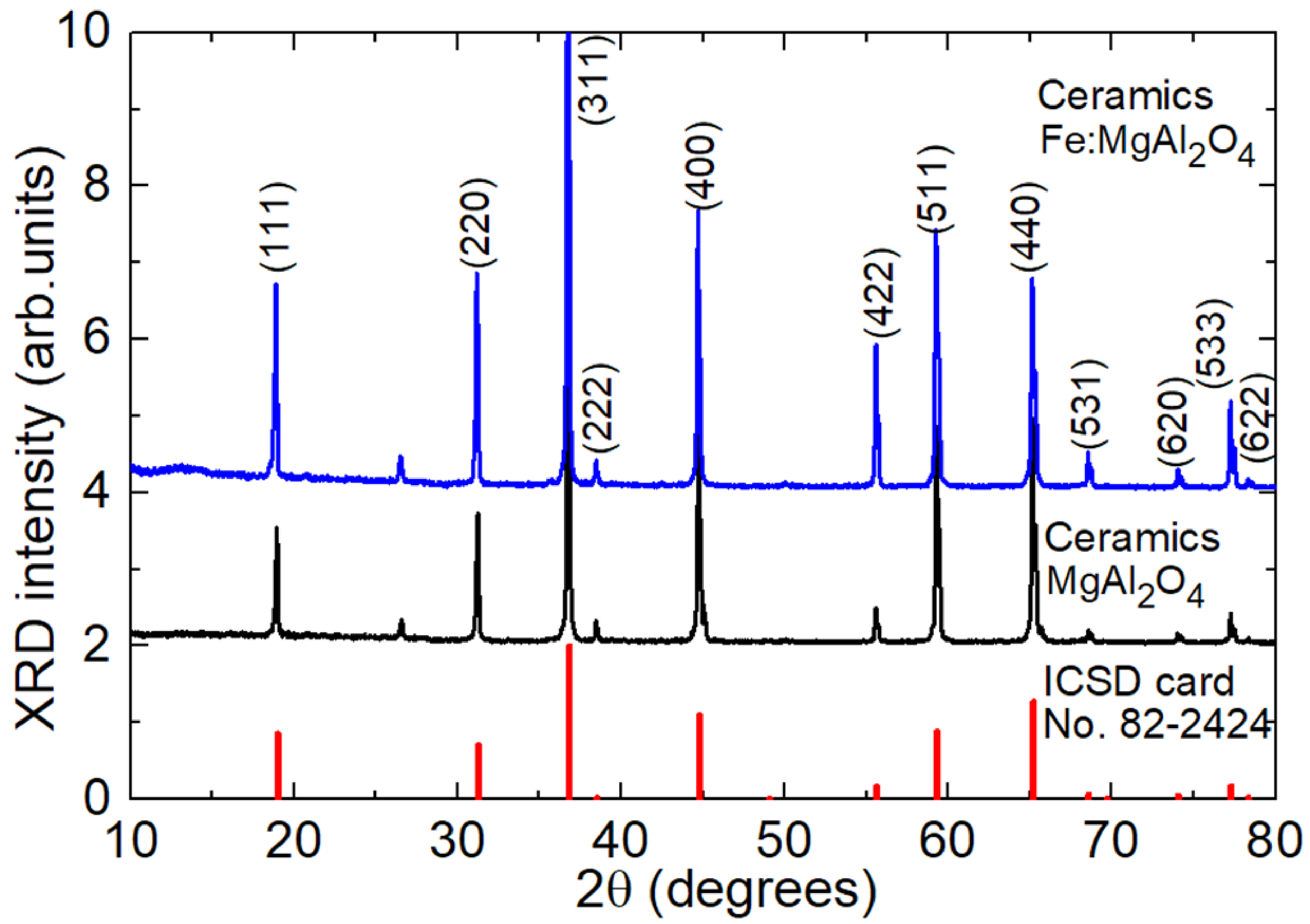
XRD intensity (arb.units)
2θ (degrees)
0
2
4
6
8
10
10
20
30
40
50
60
70
80
(111)
(220)
(311)
(222)
(400)
(422)
(511)
(440)
(531)
(620)
(533)
(622)
Ceramics
Fe:MgAl$_2$O$_4$
Ceramics
MgAl$_2$O$_4$
ICSD card
No. 82-2424

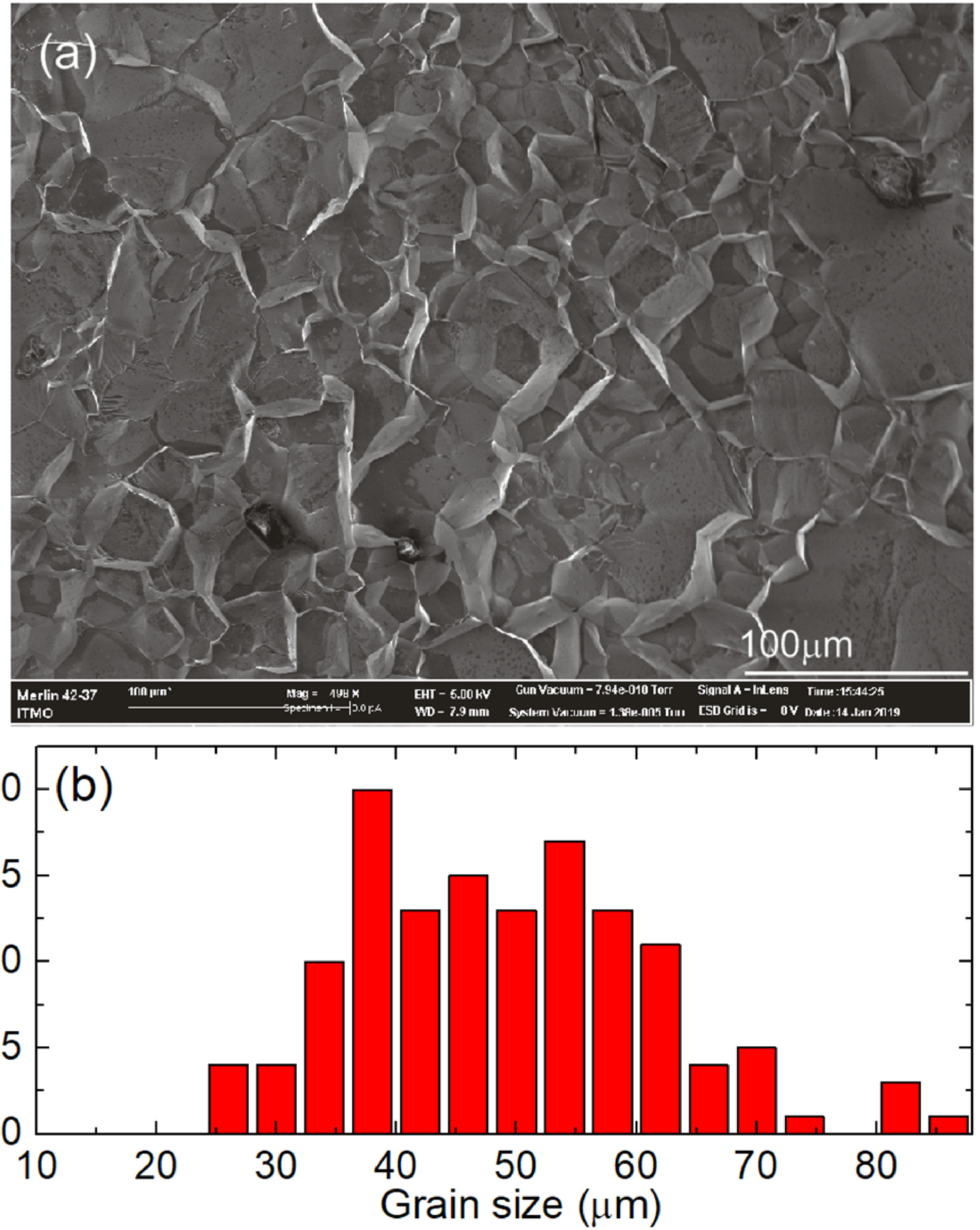
(a)
100μm
Merlin 42-37
ITMO
100 μm
Mag = 498 X
Specimen I = 0.0 pA
EHT = 5.00 kV
WD = 7.9 mm
Gun Vacuum = 7.94e-010 Torr
System Vacuum = 1.38e-005 Torr
Signal A = InLens
ESD Grid is = 0 V
Time :15:44:25
Date :14 Jan 2019
(b)
Number of grains
0
5
10
15
20
10
20
30
40
50
60
70
80
Grain size (μm)

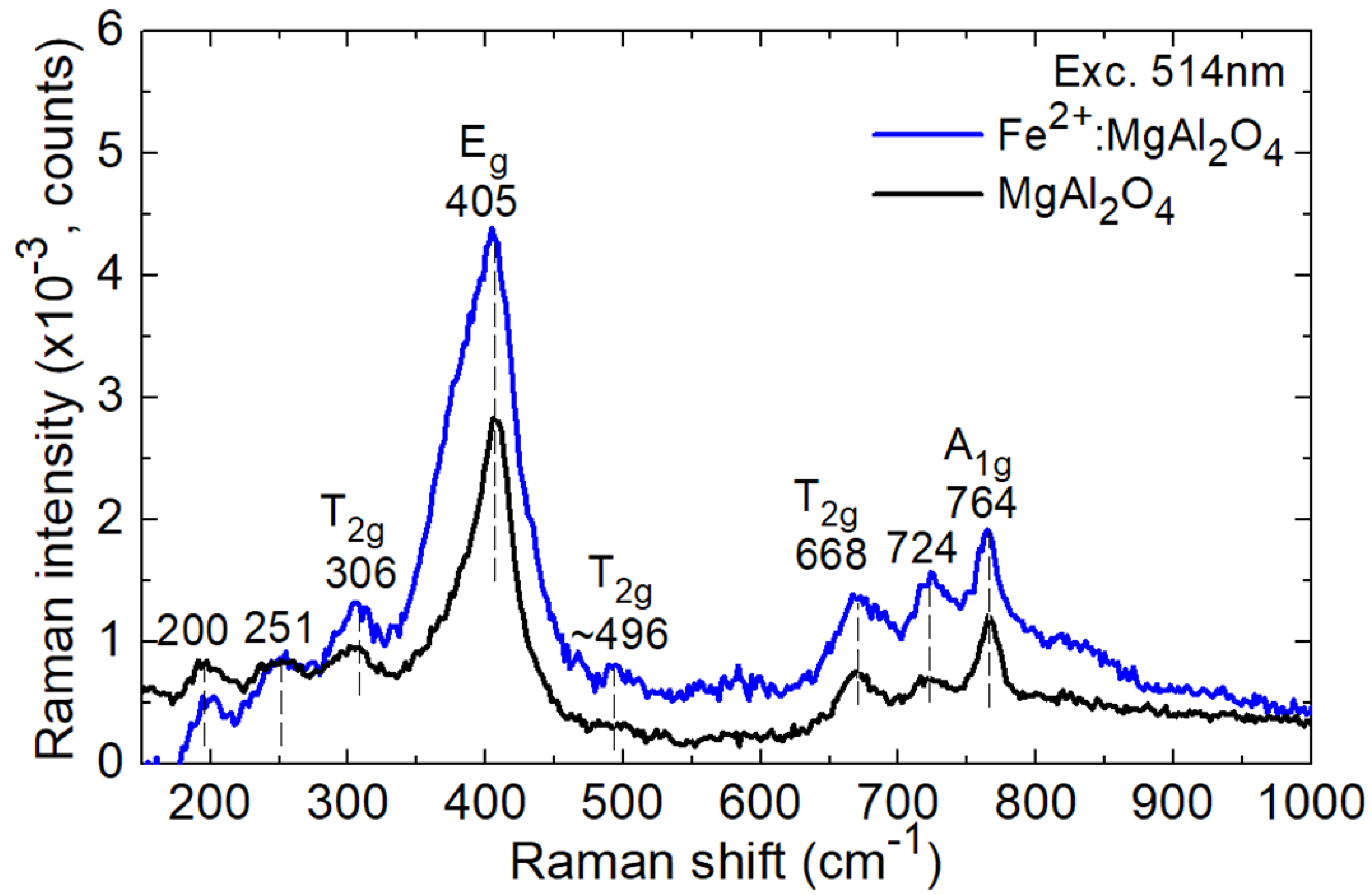
Raman intensity (x10^{-3}, counts)
Raman shift (cm^{-1})
Exc. 514nm
Fe^{2+}:MgAl$_2$O$_4$
MgAl$_2$O$_4$
E$_g$
405
T$_{2g}$
306
200
251
T$_{2g}$
~496
T$_{2g}$
668
724
A$_{1g}$
764
0
1
2
3
4
5
6
200
300
400
500
600
700
800
900
1000

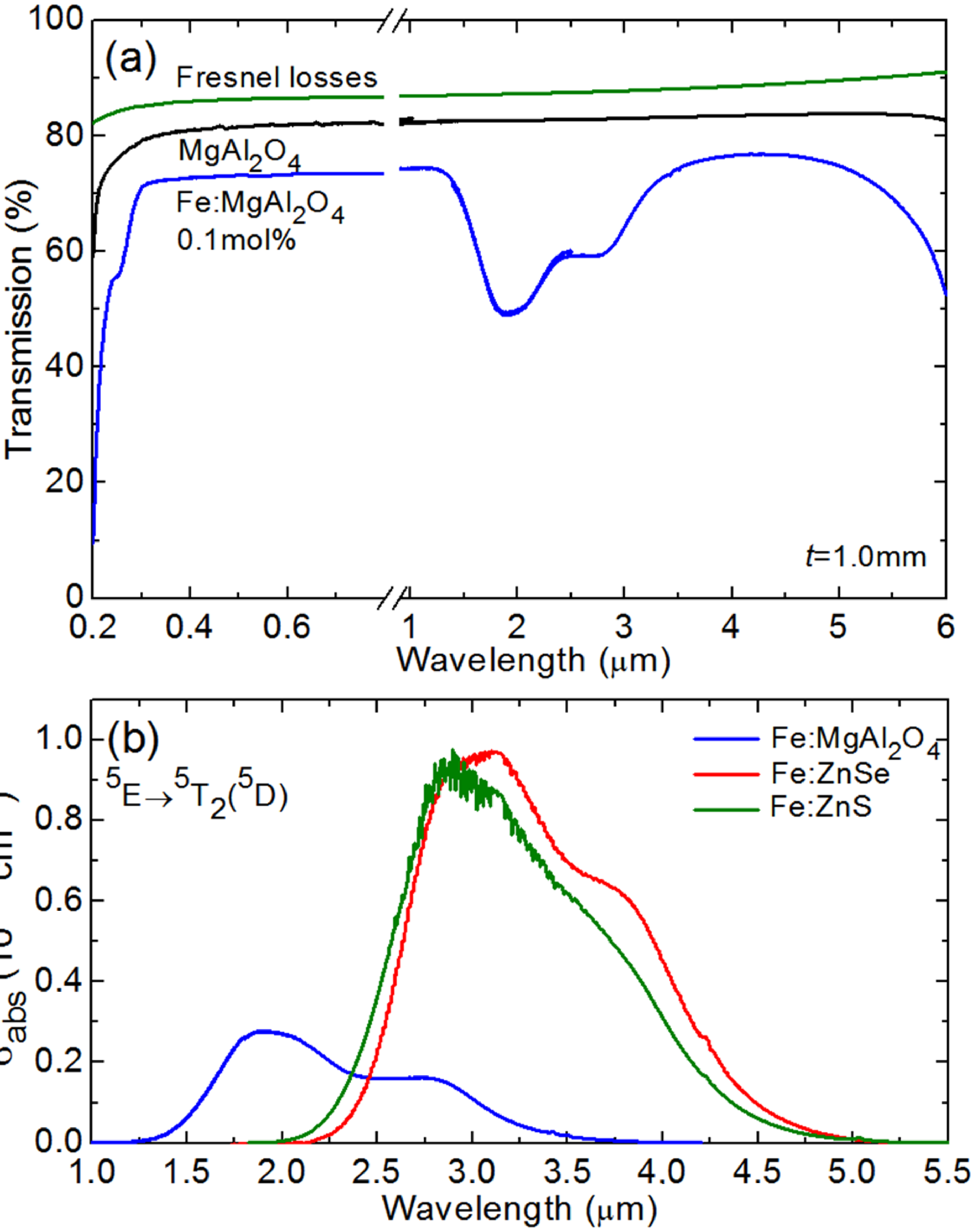
(a)
Fresnel losses
MgAl2O4
Fe:MgAl2O4
0.1mol%
t=1.0mm
Transmission (%)
100
80
60
40
20
0
0.2
0.4
0.6
1
2
3
4
5
6
Wavelength (μm)
(b)
5E→5T2(5D)
Fe:MgAl2O4
Fe:ZnSe
Fe:ZnS
σabs (10-18cm-2)
1.0
0.8
0.6
0.4
0.2
0.0
1.0
1.5
2.0
2.5
3.0
3.5
4.0
4.5
5.0
5.5
Wavelength (μm)

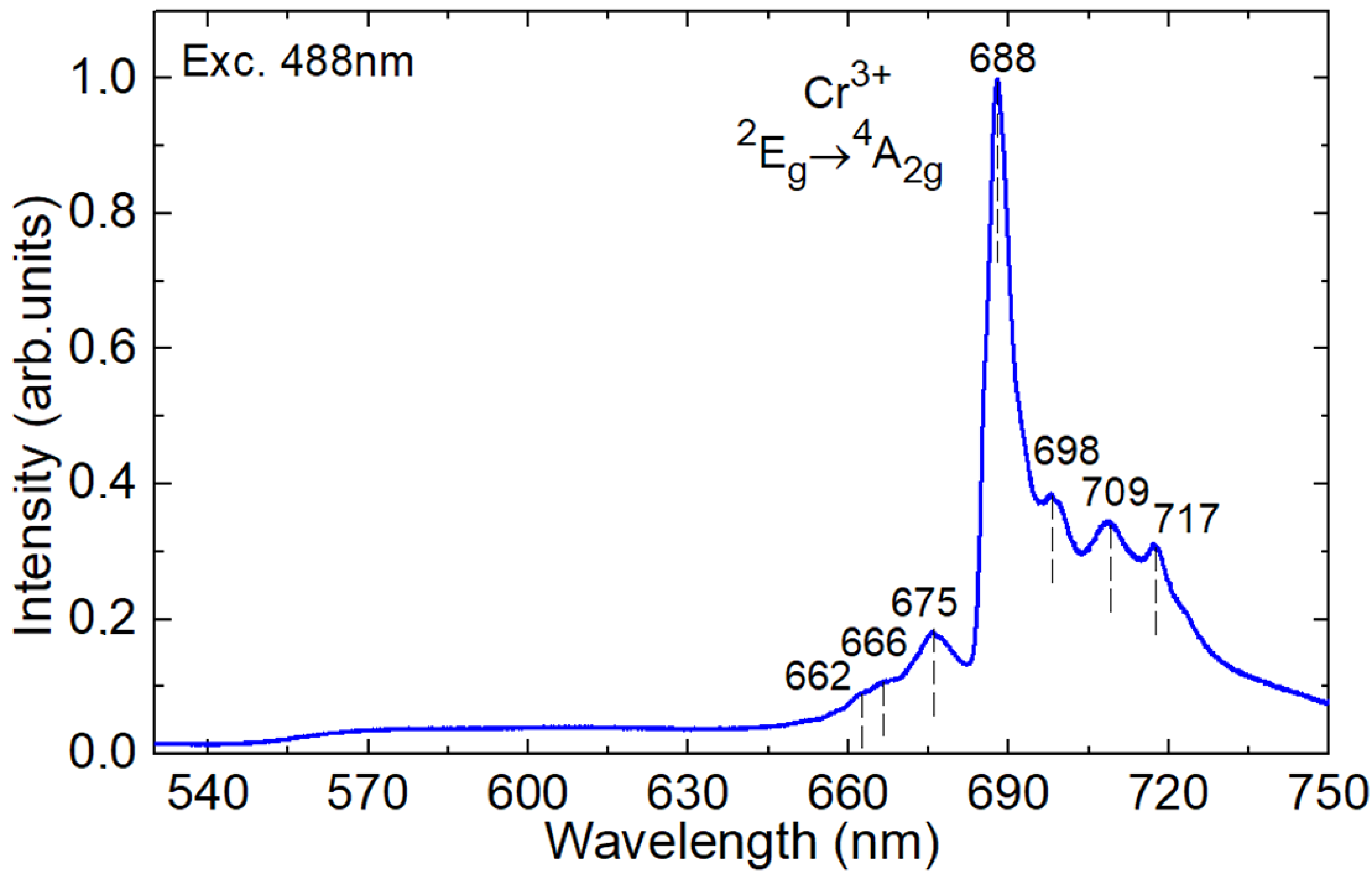
Exc. 488nm
Cr^{3+}
$^2E_g \rightarrow ^4A_{2g}$
688
698
709
717
675
666
662
Intensity (arb.units)
0.0
0.2
0.4
0.6
0.8
1.0
540
570
600
630
660
690
720
750
Wavelength (nm)

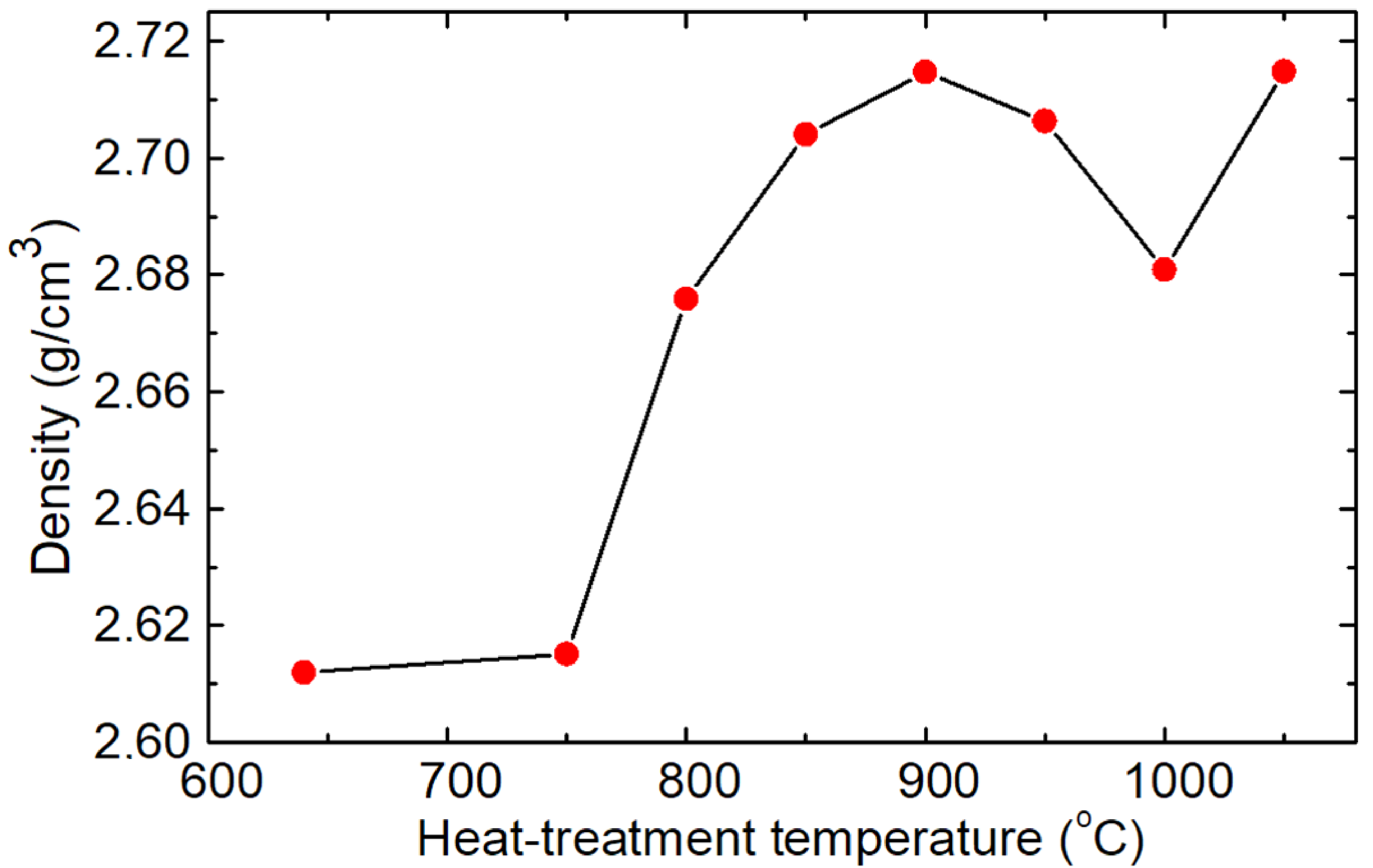
Density (g/cm^3)
2.72
2.70
2.68
2.66
2.64
2.62
2.60
600
700
800
900
1000
Heat-treatment temperature (°C)

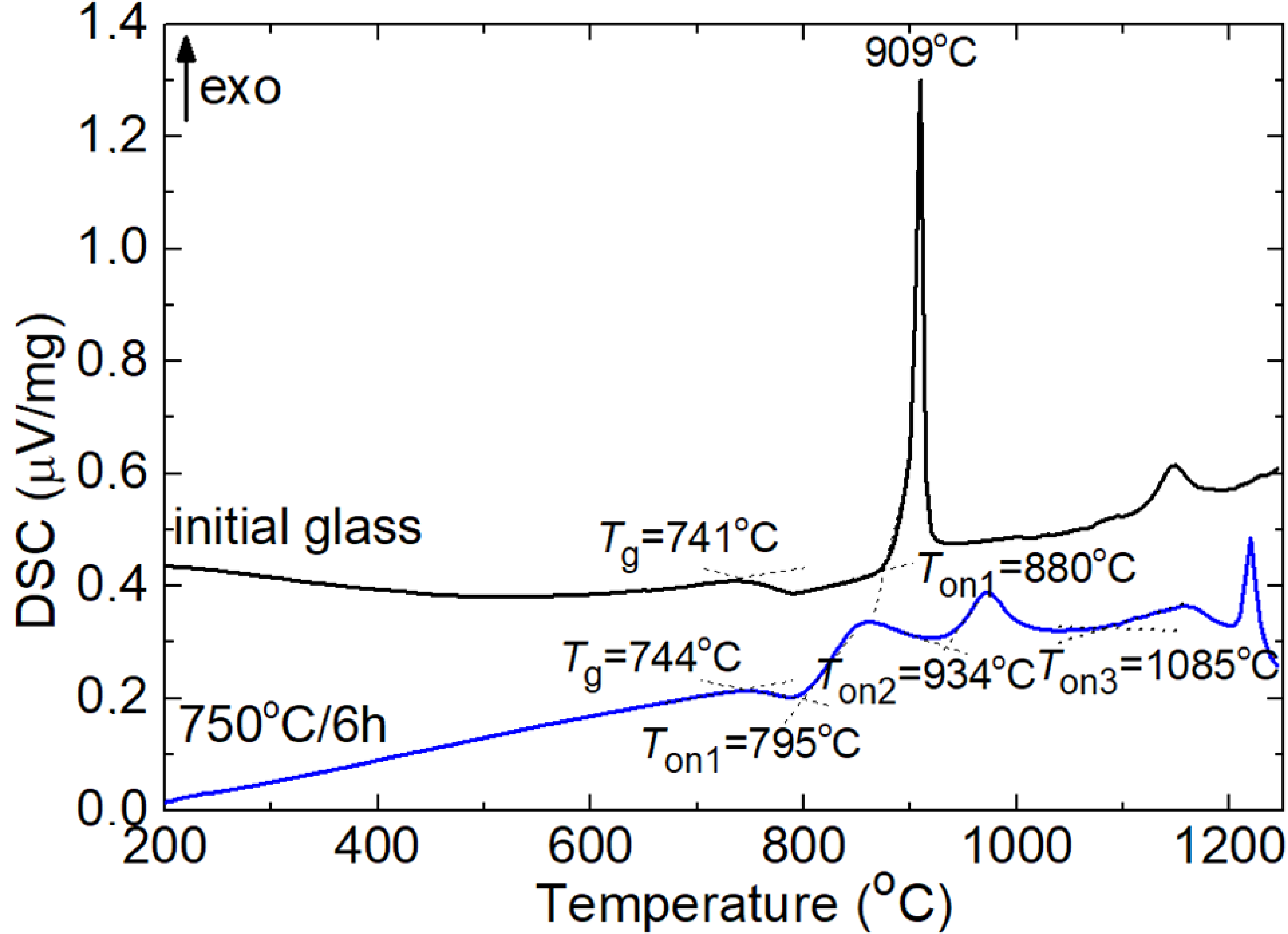

DSC (μV/mg)
1.4
1.2
1.0
0.8
0.6
0.4
0.2
0.0
200
400
600
800
1000
1200
Temperature (°C)
exo
909°C
initial glass
T_g=741°C
T_{on1}=880°C
T_g=744°C
T_{on2}=934°C
T_{on3}=1085°C
750°C/6h
T_{on1}=795°C

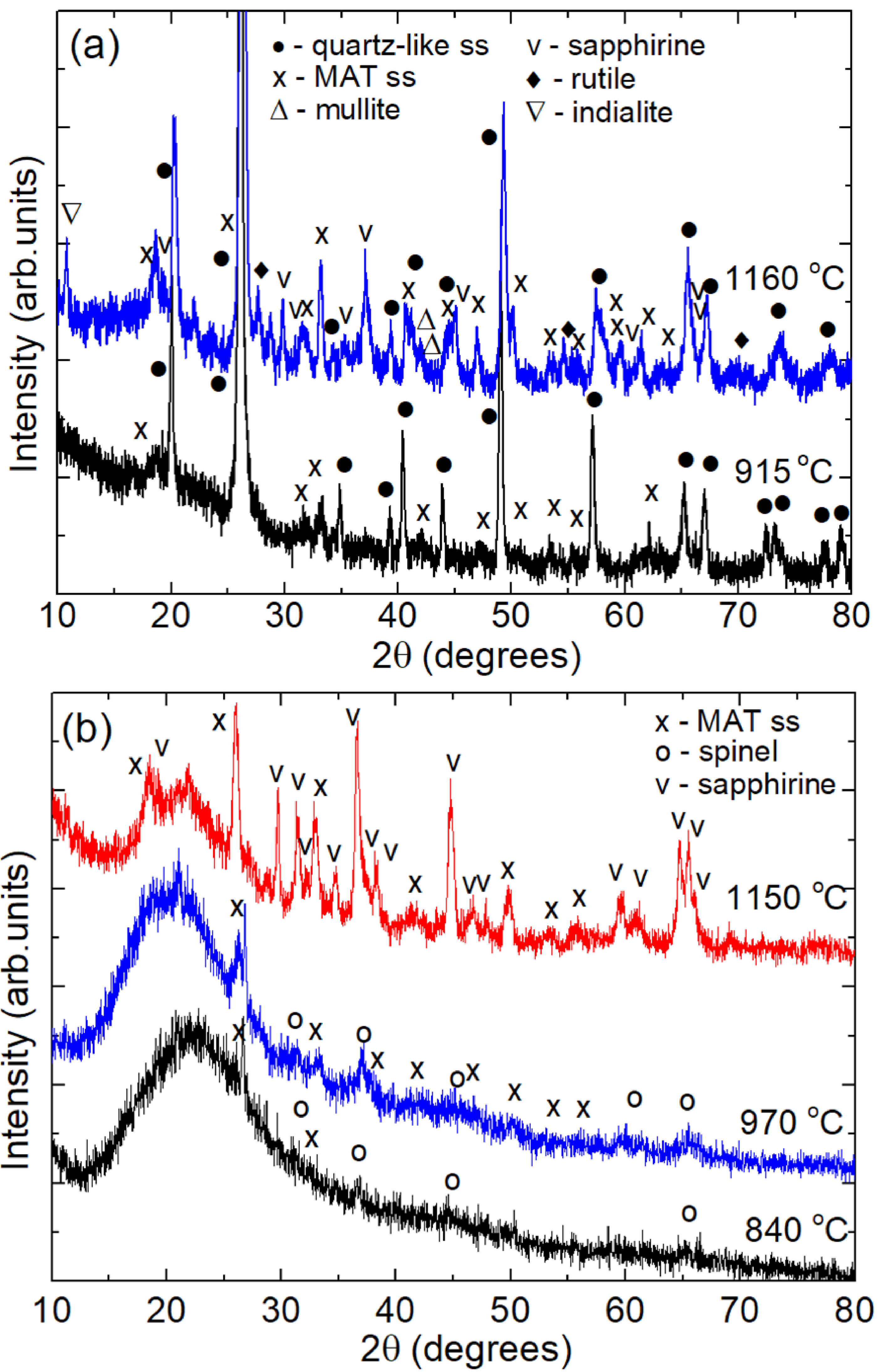
(a)
● - quartz-like ss
x - MAT ss
Δ - mullite
v - sapphirine
◆ - rutile
∇ - indialite
1160 °C
915 °C
Intensity (arb.units)
2θ (degrees)
10
20
30
40
50
60
70
80
(b)
x - MAT ss
o - spinel
v - sapphirine
1150 °C
970 °C
840 °C
Intensity (arb.units)
2θ (degrees)
10
20
30
40
50
60
70
80

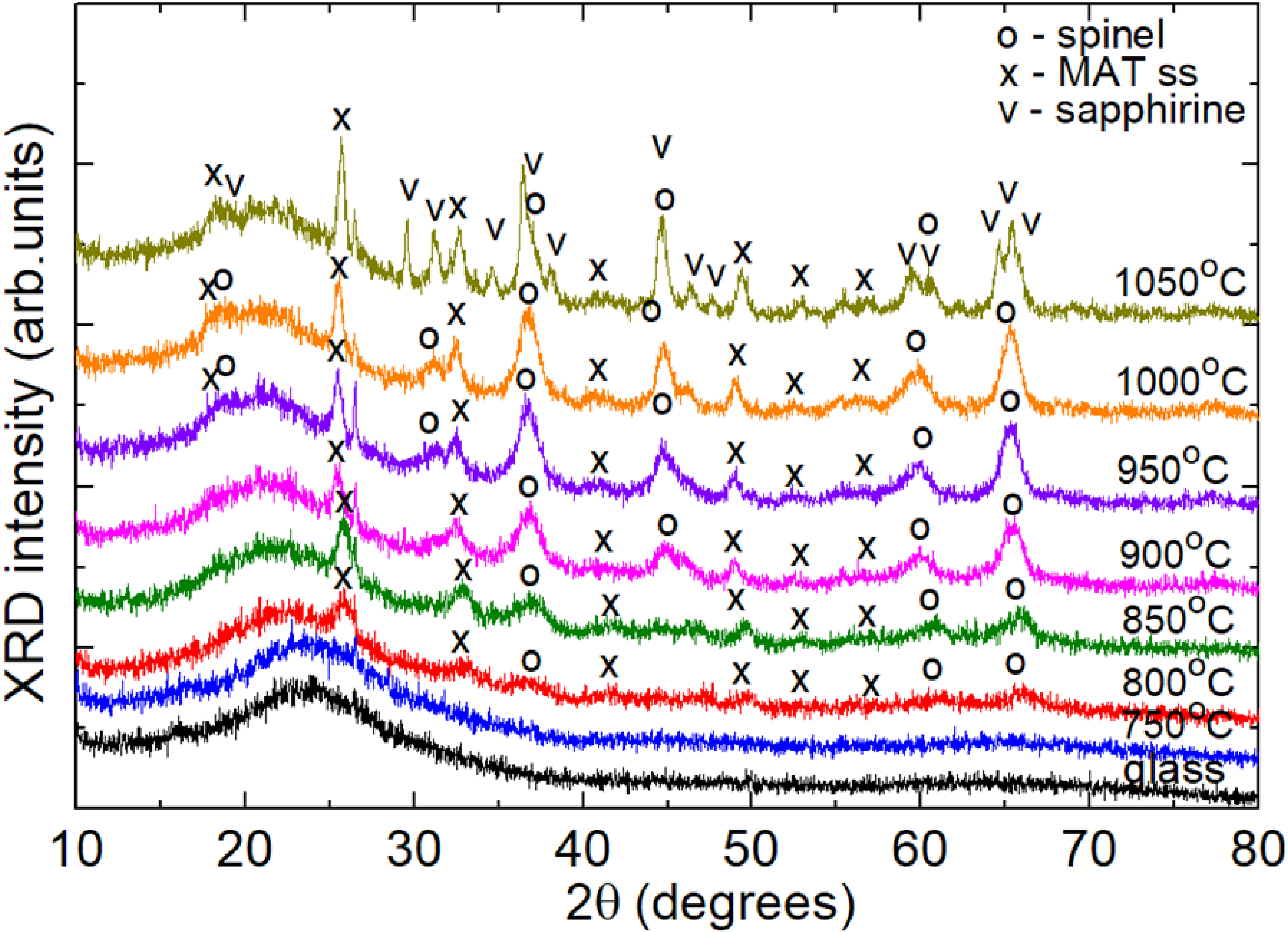
o - spinel
x - MAT ss
v - sapphirine
1050°C
1000°C
950°C
900°C
850°C
800°C
750°C
glass
XRD intensity (arb.units)
2θ (degrees)
10
20
30
40
50
60
70
80

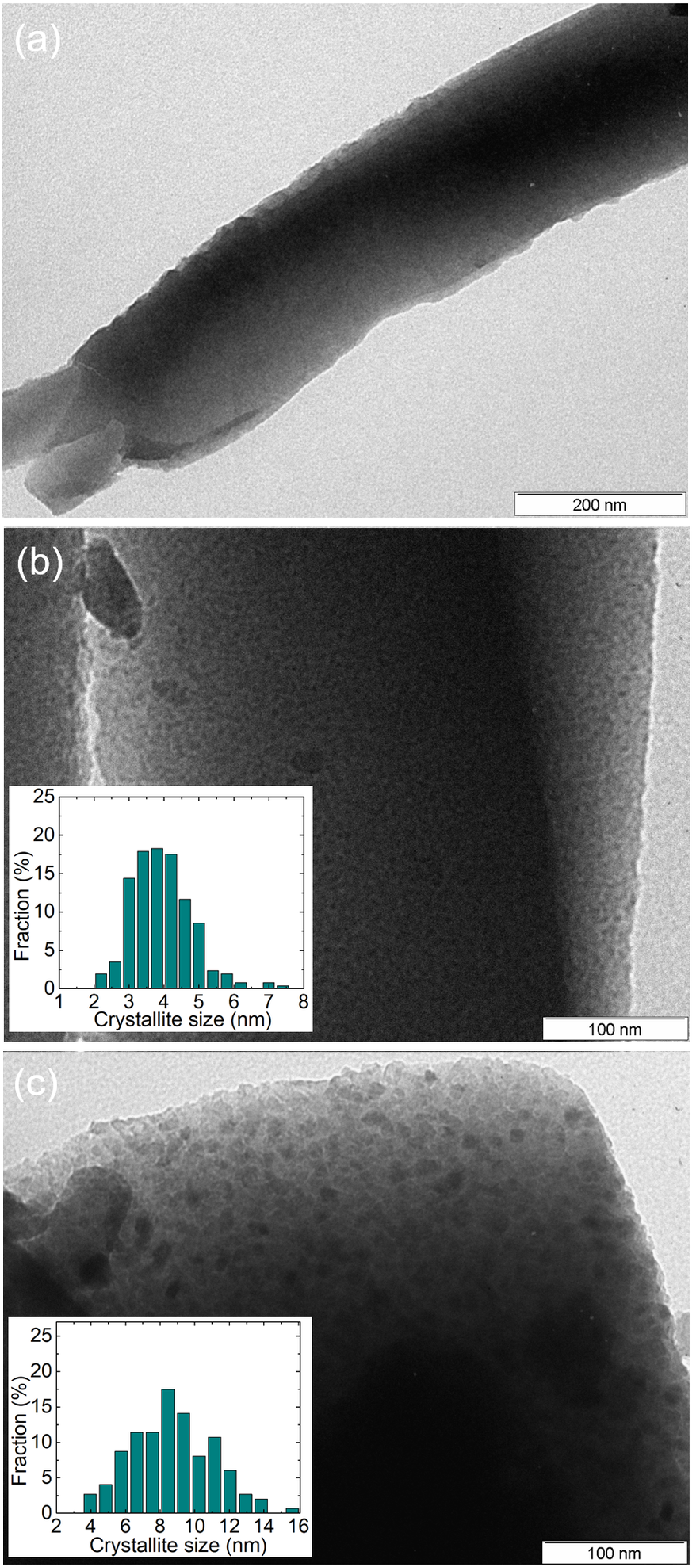
(a)
200 nm
(b)
Fraction (%)
0
5
10
15
20
25
1
2
3
4
5
6
7
8
Crystallite size (nm)
100 nm
(c)
Fraction (%)
0
5
10
15
20
25
2
4
6
8
10
12
14
16
Crystallite size (nm)
100 nm

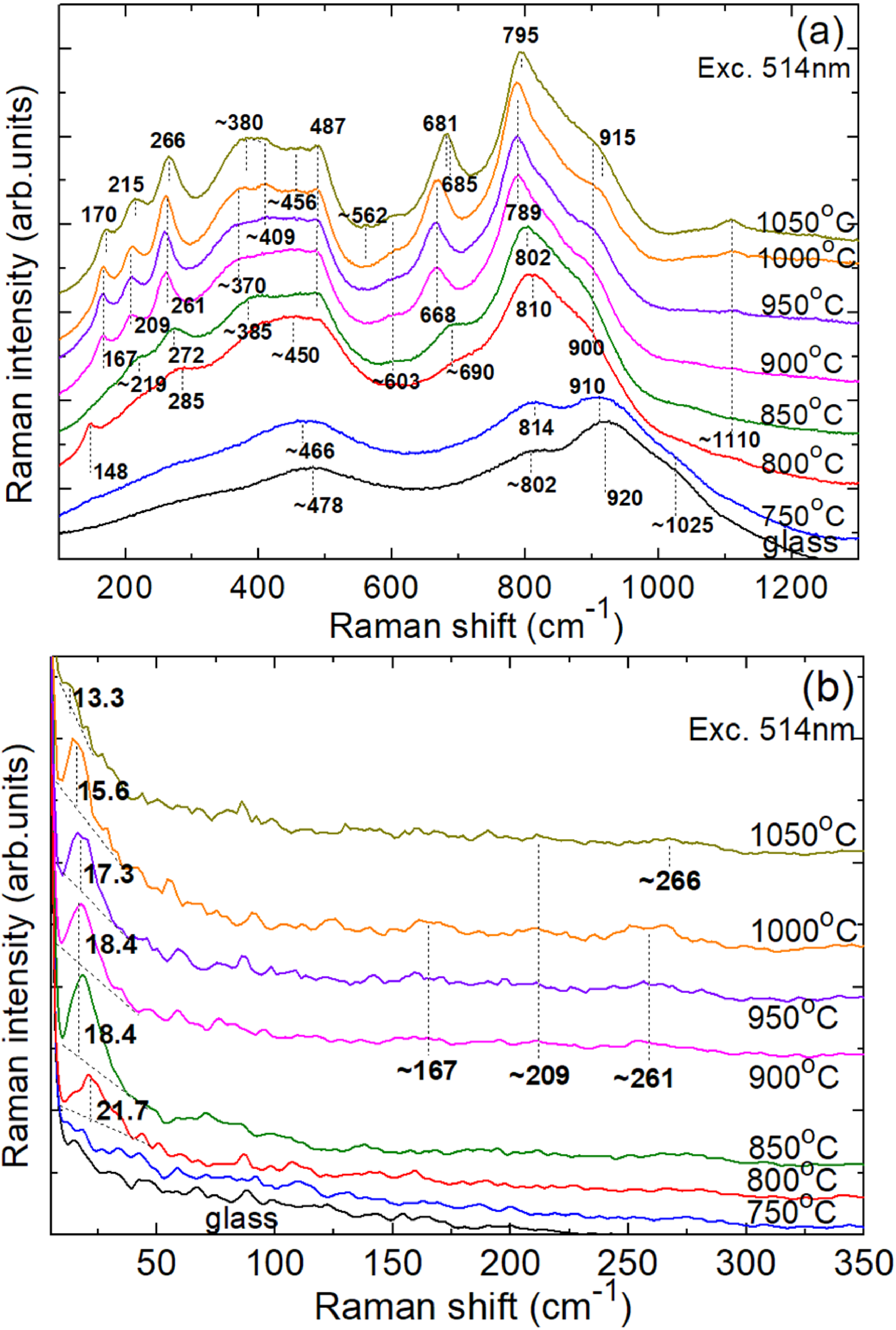
(a)
Exc. 514nm
Raman intensity (arb.units)
Raman shift (cm^{-1})
795
~380
487
681
915
266
215
170
685
~456
~562
789
~409
802
~370
261
209
668
810
~385
167
272
~450
900
~219
285
~603
~690
910
148
~466
814
~478
~802
920
~1110
~1025
1050^{o}C
1000^{o}C
950^{o}C
900^{o}C
850^{o}C
800^{o}C
750^{o}C
glass
200
400
600
800
1000
1200
(b)
Exc. 514nm
Raman intensity (arb.units)
Raman shift (cm^{-1})
13.3
15.6
17.3
18.4
18.4
21.7
~266
~167
~209
~261
1050^{o}C
1000^{o}C
950^{o}C
900^{o}C
850^{o}C
800^{o}C
750^{o}C
glass
50
100
150
200
250
300
350

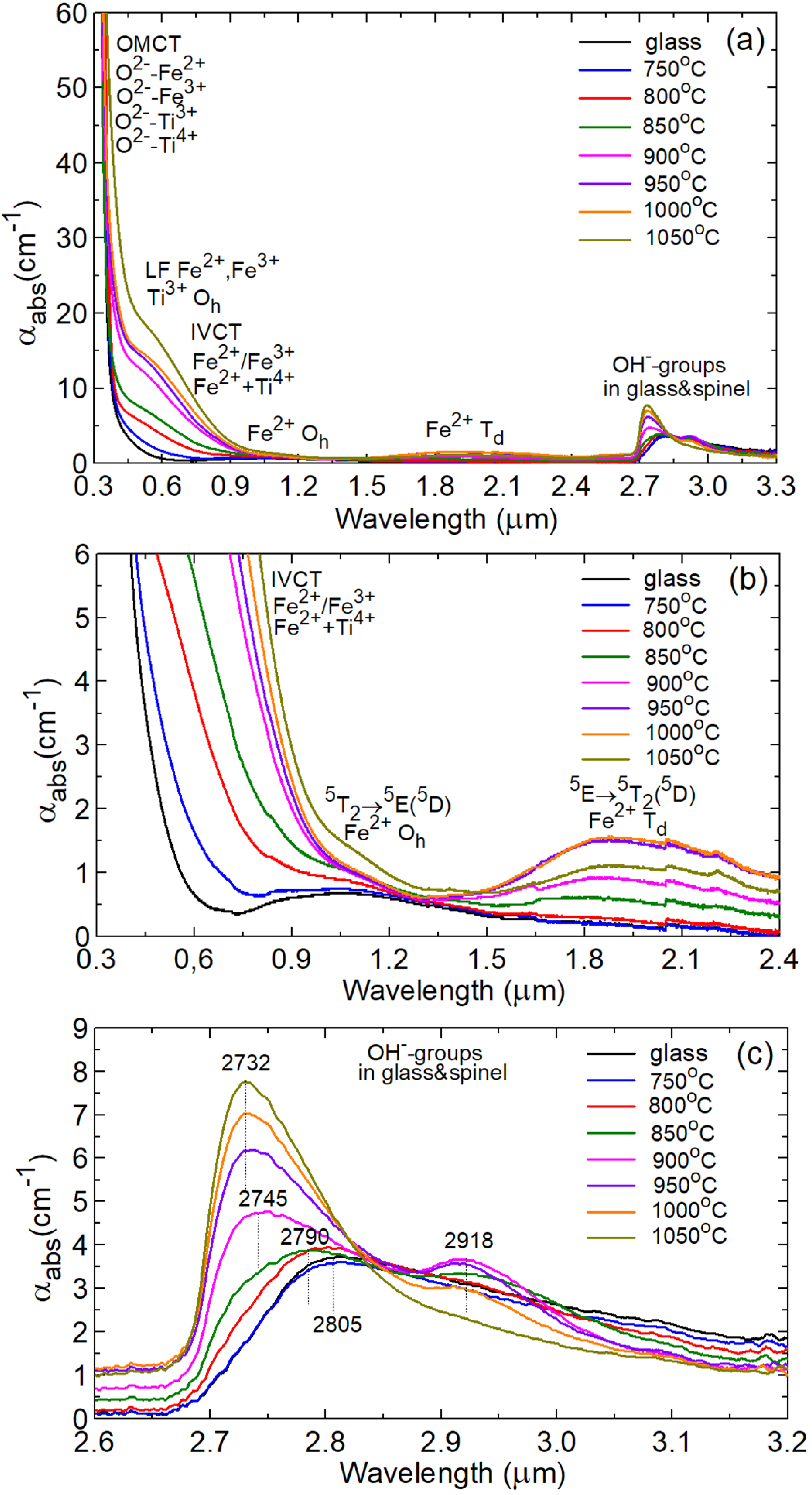
(a)
αabs(cm-1)
Wavelength (μm)
OMCT
O2- -Fe2+
O2- -Fe3+
O2- -Ti3+
O2- -Ti4+
LF Fe2+,Fe3+
Ti3+ Oh
IVCT
Fe2+/Fe3+
Fe2++Ti4+
Fe2+ Oh
Fe2+ Td
OH- -groups
in glass&spinel
glass
750oC
800oC
850oC
900oC
950oC
1000oC
1050oC
0
10
20
30
40
50
60
0.3
0.6
0.9
1.2
1.5
1.8
2.1
2.4
2.7
3.0
3.3
(b)
αabs(cm-1)
Wavelength (μm)
IVCT
Fe2+/Fe3+
Fe2++Ti4+
5T2→5E(5D)
Fe2+ Oh
5E→5T2(5D)
Fe2+ Td
glass
750oC
800oC
850oC
900oC
950oC
1000oC
1050oC
0
1
2
3
4
5
6
0.3
0,6
0.9
1.2
1.5
1.8
2.1
2.4
(c)
αabs(cm-1)
Wavelength (μm)
OH- -groups
in glass&spinel
2732
2745
2790
2805
2918
glass
750oC
800oC
850oC
900oC
950oC
1000oC
1050oC
0
1
2
3
4
5
6
7
8
9
2.6
2.7
2.8
2.9
3.0
3.1
3.2

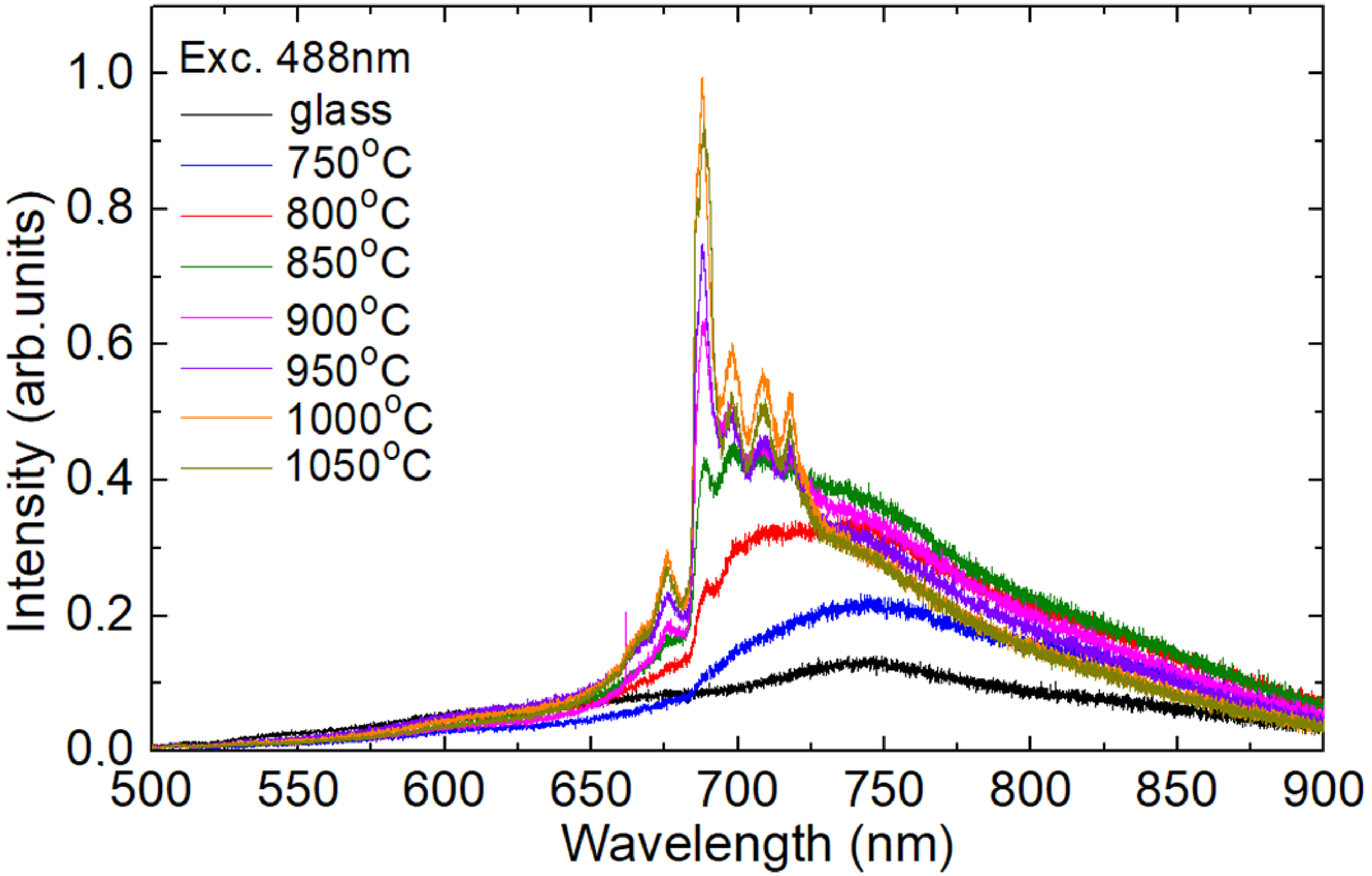
Exc. 488nm
glass
750°C
800°C
850°C
900°C
950°C
1000°C
1050°C
Intensity (arb.units)
0.0
0.2
0.4
0.6
0.8
1.0
Wavelength (nm)
500
550
600
650
700
750
800
850
900

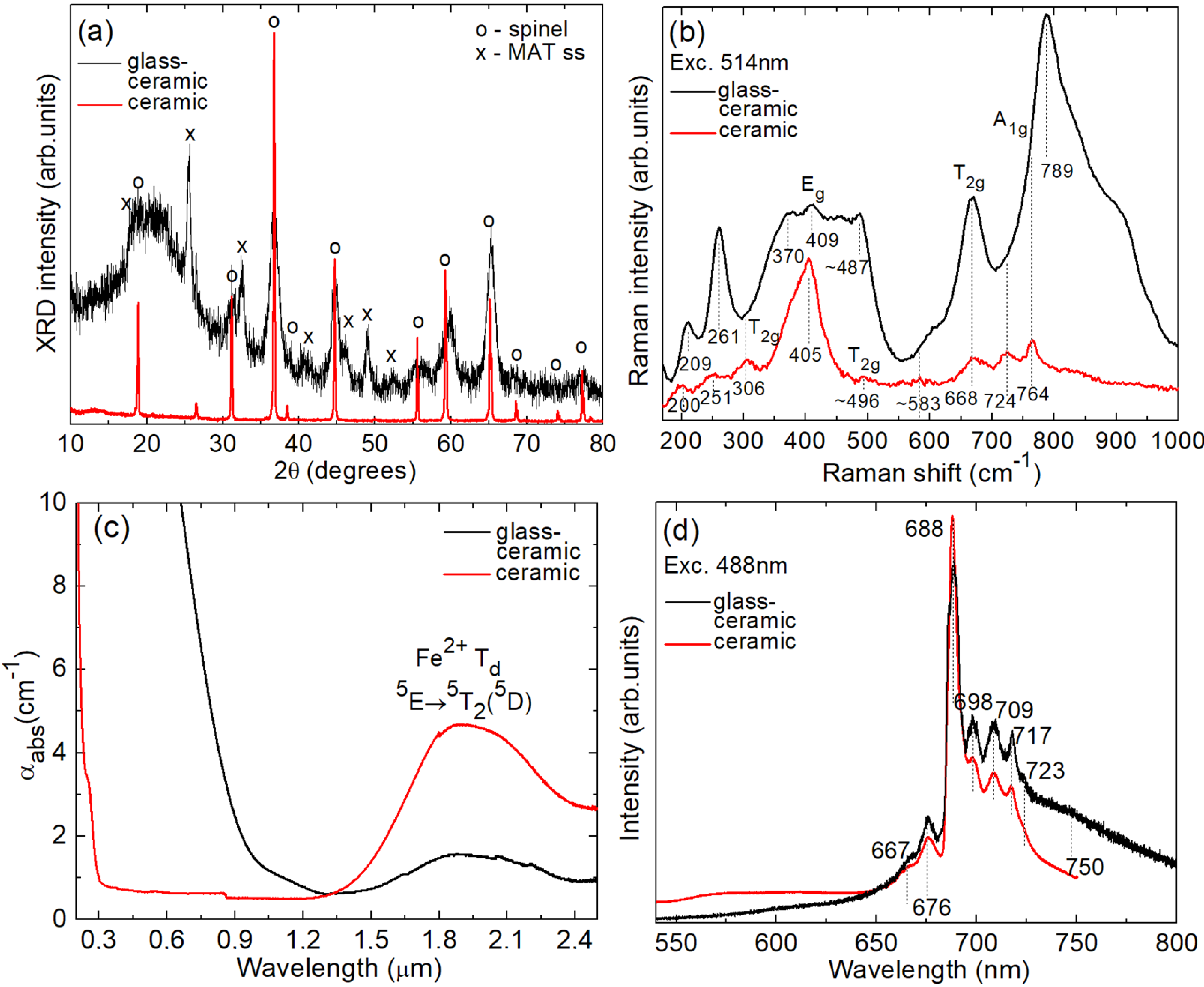
(a)
o - spinel
x - MAT ss
glass-ceramic
ceramic
XRD intensity (arb.units)
2θ (degrees)
10
20
30
40
50
60
70
80
(b)
Exc. 514nm
glass-ceramic
ceramic
Raman intensity (arb.units)
Raman shift (cm^{-1})
E_g
T_{2g}
A_{1g}
T_{2g}
T_{2g}
209
261
370
409
~487
789
200
251
306
405
~496
~583
668
724
764
200
300
400
500
600
700
800
900
1000
(c)
glass-ceramic
ceramic
Fe^{2+} T_d
$^5E \rightarrow {}^5T_2(^5D)$
α_{abs}(cm^{-1})
Wavelength (μm)
0
2
4
6
8
10
0.3
0.6
0.9
1.2
1.5
1.8
2.1
2.4
(d)
Exc. 488nm
glass-ceramic
ceramic
Intensity (arb.units)
Wavelength (nm)
688
698
709
717
723
667
676
750
550
600
650
700
750
800

Table 1. Mean size of nanocrystals *D* in transparent GCs estimated by different methods* and the unit-cell parameter of spinel nanocrystals *a*.

Heat-treatment regime	XRD			Raman	TEM
	Spinel		MAT		
	a, Å	D_{XRD}, Å	D_{XRD}, Å	D_{Raman}, Å	D_{TEM}, Å
750 °C/6 h + 800 °C/6 h	8.002	37	64	98	-
750 °C/6 h + 850 °C/6 h	8.020	41	103	115	-
750 °C/6 h + 900 °C/6 h	8.074	60	127	115	-
750 °C/6 h + 950 °C/6 h	8.079	74	146	124	64
750 °C/6 h + 1000 °C/6 h	8.079	74	206	137	-

*D_{XRD} – size determined from the XRD studies using the Scherrer formula, Eq. (1); D_{Raman} – size determined from small-frequency Raman spectra, Eq. (4); D_{TEM} – size determined from TEM images.